International Journal of Solids and Structures 49 (2012) 658–671

Contents lists available at SciVerse ScienceDirect

International Journal of Solids and Structures

journal homepage: www.elsevier.com/locate/ijsolstr

Spherical ceramic pebbles subjected to multiple non-concentrated surface loads

Shuo Zhao [a,b], Yixiang Gan [c], Marc Kamlah [b,*]

[a] College of Mechanical and Electronic Engineering, Hebei University of Science and Technology, Shijiazhuang, Hebei 050018, China
[b] Institute for Applied Materials, Karlsruhe Institute of Technology, D-76344 Eggenstein-Leopoldshafen, Germany
[c] Particles and Grains Laboratory, School of Civil Engineering, The University of Sydney, NSW 2006, Australia

ARTICLE INFO

Article history:
Received 15 March 2011
Received in revised form 7 November 2011
Available online 23 November 2011

Keywords:
Ceramic pebbles
Multiple loads
Elastic sphere
Spherical isotropy
Stress analysis

ABSTRACT

This paper presents an analytical solution for the stress distributions within spherical ceramic pebbles subjected to multiple surface loads along different directions. The method of solution employs a displacement approach together with the Fourier associated Legendre expansion for piecewise boundary loads. The solution corresponds to spherically isotropic elastic spheres. The classical solution for isotropic spheres subjected diametral point loads is recovered as a special case of our solution. For the isotropic pebbles under consideration, stresses within spheres are numerically evaluated. The results show that the number of loads does have significant influence on the maximum tensile stress inside the sphere. Moreover, the applicability of solutions using the series expansion method for stresses near surface load areas is also examined. The stresses evaluated with large enough number of terms agree quite well with those derived from FEM simulations, except around the edge of circle load area.

1. Introduction

In the development of fusion technology, ceramic pebbles constituting pebble beds will be used in helium cooled pebble bed (HCPB) blankets (Giancarli et al., 2000; Poitevin et al., 2005; Boccaccini et al., 2009). The two kinds of ceramic pebbles under consideration are: lithium orthosilicate (Li_4SiO_4) pebbles having a good spherical shape (Knitter, 2003; Knitter et al., 2007) and lithium metatitanate (Li_2TiO_3) pebbles having an ellipsoidal shape (van der Laan and Muis, 1999; Tsuchiya et al., 2005). Individual pebbles might be crushed due to thermal mismatch between pebbles and their confinement walls. The crushed pebbles will lead to negative consequence. For instance, the fragments of crushed pebbles might block the evacuation of helium gas which brings the generated tritium away for further fusion reaction, i.e., deuterium–tritium reaction. Therefore, it is essential to study the mechanical strength of the pebbles.

The strength of pebbles is considered to be a material property characterizing when a pebble will fail. This pebble property has not yet been identified in experiments although many crush tests have been carried out where pebbles are crushed between two parallel plates, as shown in Fig. 1 (1). Crush loads at which pebbles fail are derived from the tests. The crush load is related to the pebble strength in this given configuration. However, for pebbles in pebble beds where each pebble has many contacts with neighboring pebbles, as shown in Fig. 1 (2), the crush load from crush tests cannot predict when a pebble will fail under multiple contact loads. Essentially, pebble failure should be dominated by the stress field, i.e., pebble strength is some kind of critical stress, such as maximum tensile or shear stress. This work is not intended to identify its strength, but to derive the stress field inside a pebble in pebble beds. Note that Li_4SiO_4 pebbles under consideration have a good sphericity (Löbbecke and Knitter, 2009), and can be considered as a solid sphere consequently.

The number of neighboring contacts is defined as the coordination number N_c. There are some analytical solutions for stress field in an elastic sphere with different N_c. For $N_c = 1$, Dean et al. (1952) have studied a sphere under a single load which is equilibrated by body force. The single load is represented by uniform pressure. For diametral load, i.e., $N_c = 2$, stress field in an isotropic sphere has been derived by Hiramatsu and Oka (1966), and that in a spherically isotropic sphere has been derived by Chau and Wei (1999). Evaluation of their solution for isotropic sphere subjected to uniform pressure shows the influence of Poisson's ratio on the maximum tensile stress inside the sphere. A smaller Poisson's ratio leads to a higher maximum tensile stress while stresses around the sphere center are almost independent of the Poisson's ratio (see Chau and Wei, 1999, Fig. 4). The Poisson's ratio does not appear in the solution by Dean et al. (1952) for $N_c = 1$, and the superimposed results using this solution for diametral load (see Gundepudi et al., 1997, Fig. 4) show good agreement only near the sphere center. For $N_c > 2$, a solution for an elastic sphere subjected to multiple concentrated loads has been obtained by Guerrero and Turteltaub (1972). However, this solution cannot represent real contact problems with a finite contact area. No

* Corresponding author. Tel.: +49 721 608 25860; fax: +49 721 608 22347.
E-mail address: marc.kamlah@kit.edu (M. Kamlah).

0020-7683/$ - see front matter © 2011 Elsevier Ltd. All rights reserved.
doi:10.1016/j.ijsolstr.2011.11.009

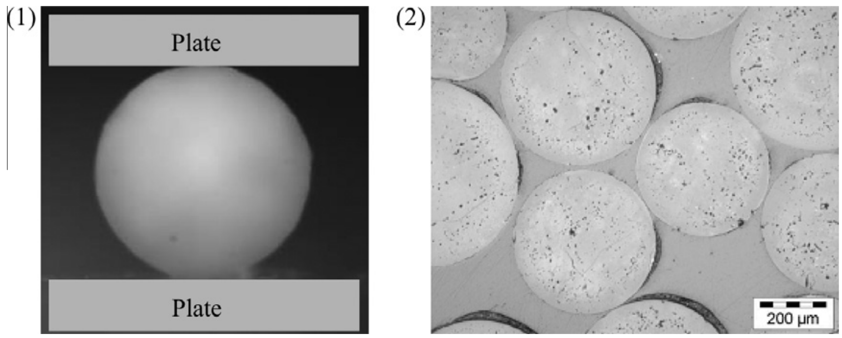

Fig. 1. (1) crush tests for single pebbles; (2) pebbles in a pebble bed (Löbbecke and Knitter, 2009).

complete solution has been reported for stress field in a sphere subjected to multiple contacts with a finite contact area. On the other hand, superimposition of solutions for $N_c = 1$ or $N_c = 2$ has been used to solve special problems for $N_c > 2$ (Gundepudi et al., 1997; Russell et al., 2009). The limit of the superimposed method using the solution for $N_c = 1$ will be the inaccuracy around where maximum tensile stress inside sphere appears. The limit of the superimposed method using the solution for $N_c = 2$ is that N_c should be even and contact forces must be pairs of diametral loads.

In this paper, we derive an analytical solution for stress distributions within a spherically isotropic elastic sphere in equilibrium subjected to multiple normal surface loads along different directions. Stresses tangential to the surface are taken to be zero, and the body force is neglected. The general theory for a spherically isotropic medium has been studied by Hu (1954) and Chen (1966). This theory is suitable for considering multiple mechanical loadings to the surface of a solid sphere. Chen (1966) has further studied problems taking into account body forces. There have been already some theoretical analyses by Ding and Ren (1991), Chau (1995, 1998) and Chau and Wei (1999) for spherically isotropic spheres. The method of solutions used in this work follows the steps of Hu (1954), Ding and Ren (1991), and Chau and Wei (1999). We make use of their methods, such as the proposed displacement potentials (Hu, 1954) and introduced variables (Ding and Ren, 1991), and conclusions, such as the requirements on the roots (Chau and Wei, 1999) (see Section 2.5). New displacement functions incorporating the direction of loads are proposed in this paper. Correspondingly, the piecewise surface load functions are expanded with Fourier associated Legendre functions. Each load is distributed across a circular surface area. Note that the pebbles mentioned before are of isotropic material which is a special case of a spherically isotropic material. The solution can be reduced to the case for isotropic spheres corresponding to spherical ceramic pebbles, i.e., Li_4SiO_4. Numerical evaluation will be thus performed mainly for isotropic spheres. The main focus here will be the effect of N_c on the maximum tensile stress in a pebble. In literature one finds criteria for the strength of spheres for which other kinds of stresses such as the maximum shear stress are of importance (Russell and Muir Wood, 2009; Russell et al., 2009). The failure criterion for the pebbles mentioned above is subject of a separate paper (Zhao et al., submitted for publication).

This paper is organized as follows. In Section 2, first the general theory and problem formulation for spherically isotropic spheres is presented. In Section 2.4, the displacement potential functions used in this work are described. Then the solution methodology of the boundary value problem (2.5–2.7) will be discussed followed by the final solution (2.8) for the stress distribution in the form of an infinite series. In Section 3, the numerical evaluation with a finite number of terms in the solution mainly for isotropic spherical pebbles is presented. Maximum tensile stresses along a loading axis are calculated for $N_c = 2,4,6$, respectively. Moreover, Hertz contact theory and FEM simulation results have been used to validate the present solution. The minimum number of terms needed in the series solution to obtain a specific accuracy is investigated in Section 4. Section 5 discusses the potential applicability of the present solution to the failure analysis of pebbles. Finally, the conclusions are drawn in Section 6.

2. Theory

2.1. Hooke's law

With the spherical coordinate system (r,θ,φ) as shown in Fig. 2, the relations between the components of stress $\boldsymbol{\sigma}$ and strain $\boldsymbol{\varepsilon}$ are expressed by the generalized Hooke's law for spherically isotropic spheres (Hu, 1954; Ding and Ren, 1991; Chau and Wei, 1999) as

$$\begin{aligned}
&\sigma_{\theta\theta} = (2A_{66}+A_{12})\varepsilon_{\theta\theta}+A_{12}\varepsilon_{\varphi\varphi}+A_{13}\varepsilon_{rr},\\
&\sigma_{\varphi\varphi} = A_{12}\varepsilon_{\theta\theta}+(2A_{66}+A_{12})\varepsilon_{\varphi\varphi}+A_{13}\varepsilon_{rr},\\
&\sigma_{rr} = A_{13}(\varepsilon_{\theta\theta}+\varepsilon_{\varphi\varphi})+A_{33}\varepsilon_{rr},\\
&\sigma_{\theta\varphi} = 2A_{66}\varepsilon_{\theta\varphi}, \quad \sigma_{r\theta} = 2A_{44}\varepsilon_{r\theta}, \quad \sigma_{r\varphi} = 2A_{44}\varepsilon_{r\varphi},
\end{aligned} \tag{1}$$

where

$$\begin{aligned}
&A_{12} = -\frac{E(\nu E'+\nu'^2E)}{(1+\nu)\bar{E}}, \quad A_{13} = -\frac{\nu'E'E}{\bar{E}}, \quad A_{33} = -\frac{E'^2(1-\nu)}{\bar{E}},\\
&A_{66} = \frac{E}{2(1+\nu)}, \quad A_{44} = G', \quad \bar{E} = E'(\nu-1)+2\nu'^2E.
\end{aligned} \tag{2}$$

E and E' are the Young's moduli governing the deformation in the isotropic plane and along the direction perpendicular to it, i.e., the radial direction, respectively. The corresponding Poisson's ratios are ν and ν', respectively. G' is the shear modulus governing the shear deformation in the isotropic plane perpendicular to the radial

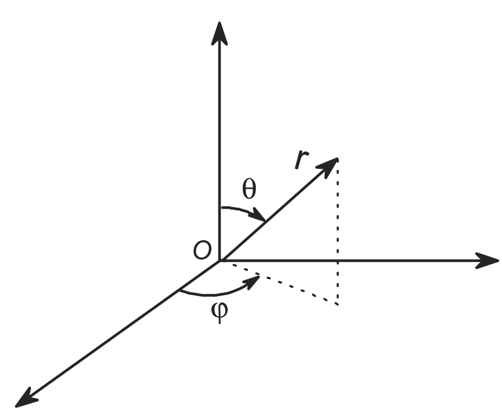

Fig. 2. Spherical coordinate system (r,θ,φ).

direction. Spherical isotropy contains isotropy as a special case. For the case of an isotropic material, the material parameters reduce to

$$E' = E, \quad \nu' = \nu, \quad G' = \frac{E}{2(1+\nu)}. \tag{3}$$

The relations between the components of small strains $\boldsymbol{\varepsilon}$, and small displacements $\boldsymbol{u}$, are expressed as

$$\begin{aligned}
&\varepsilon_{rr} = \frac{\partial u_r}{\partial r}, \quad \varepsilon_{\theta\theta} = \frac{1}{r}\frac{\partial u_\theta}{\partial \theta} + \frac{u_r}{r}, \quad \varepsilon_{\varphi\varphi} = \frac{1}{r\sin\theta}\frac{\partial u_\varphi}{\partial \varphi} + \frac{u_r}{r} + \frac{u_\theta}{r}\cot\theta,\\
&\varepsilon_{r\varphi} = \frac{1}{2}\left(\frac{1}{r\sin\theta}\frac{\partial u_r}{\partial \varphi} - \frac{u_\varphi}{r} + \frac{\partial u_\varphi}{\partial r}\right), \quad \varepsilon_{r\theta} = \frac{1}{2}\left(\frac{1}{r}\frac{\partial u_r}{\partial \theta} - \frac{u_\theta}{r} + \frac{\partial u_\theta}{\partial r}\right),\\
&\varepsilon_{\theta\varphi} = \frac{1}{2}\left(\frac{1}{r}\frac{\partial u_\varphi}{\partial \theta} - \frac{u_\varphi}{r}\cot\theta + \frac{1}{r\sin\theta}\frac{\partial u_\theta}{\partial \varphi}\right),
\end{aligned} \tag{4}$$

where u_θ, u_φ and u_r are displacements in the directions of θ, φ and r, respectively.

2.2. Equilibrium equations

The equations of equilibrium in spherical coordinates (ignoring body force) can be written as

$$\begin{aligned}
&\frac{\partial \sigma_{rr}}{\partial r} + \frac{1}{r\sin\theta}\frac{\partial \sigma_{r\varphi}}{\partial \varphi} + \frac{1}{r}\frac{\partial \sigma_{r\theta}}{\partial \theta} + \frac{2\sigma_{rr} - \sigma_{\theta\theta} - \sigma_{\varphi\varphi} + \sigma_{r\theta}\cot\theta}{r} = 0,\\
&\frac{\partial \sigma_{r\varphi}}{\partial r} + \frac{1}{r\sin\theta}\frac{\partial \sigma_{\varphi\varphi}}{\partial \varphi} + \frac{1}{r}\frac{\partial \sigma_{\theta\varphi}}{\partial \theta} + \frac{3\sigma_{r\varphi} + 2\sigma_{\theta\varphi}\cot\theta}{r} = 0,\\
&\frac{\partial \sigma_{r\theta}}{\partial r} + \frac{1}{r\sin\theta}\frac{\partial \sigma_{\theta\varphi}}{\partial \varphi} + \frac{1}{r}\frac{\partial \sigma_{\theta\theta}}{\partial \theta} + \frac{3\sigma_{r\theta} + (\sigma_{\theta\theta} - \sigma_{\varphi\varphi})\cot\theta}{r} = 0.
\end{aligned} \tag{5}$$

Substituting Eqs. (1) and (4) into (5), the equilibrium equations read as

$$\begin{aligned}
&-2(A_{12} + A_{66})\frac{\varepsilon_1}{r} + A_{13}\left(\frac{\partial \varepsilon_1}{\partial r} + \frac{2\varepsilon_1}{r} - \frac{2\varepsilon_{rr}}{r}\right) + A_{33}\left(\frac{\partial \varepsilon_{rr}}{\partial r} + \frac{2\varepsilon_{rr}}{r}\right)\\
&\quad + A_{44}\left[\frac{1}{r^2}\nabla_1^2 u_r + \frac{\partial}{\partial r}\left(\varepsilon_1 - \frac{2u_r}{r}\right)\right] = 0,\\
&\frac{A_{12}}{r\sin\theta}\frac{\partial \varepsilon_1}{\partial \varphi} + 2A_{66}\left(\frac{1}{r\sin\theta}\frac{\partial \varepsilon_{\varphi\varphi}}{\partial \varphi} + \frac{1}{r}\frac{\partial \varepsilon_{\theta\varphi}}{\partial \theta} + \frac{2\cot\theta}{r}\varepsilon_{\theta\varphi}\right)\\
&\quad + \frac{A_{13}}{r\sin\theta}\frac{\partial \varepsilon_{rr}}{\partial \varphi} + 2A_{44}\left(\frac{\partial \varepsilon_{r\varphi}}{\partial r} + \frac{3\varepsilon_{r\varphi}}{r}\right) = 0,\\
&\frac{A_{12}}{r}\frac{\partial \varepsilon_1}{\partial \theta} + 2A_{66}\left[\frac{1}{r\sin\theta}\frac{\partial \varepsilon_{\theta\varphi}}{\partial \varphi} + \frac{1}{r}\frac{\varepsilon_{\theta\theta}}{\partial \theta} + \frac{\cot\theta}{r}(\varepsilon_{\theta\theta} - \varepsilon_{\varphi\varphi})\right]\\
&\quad + \frac{A_{13}}{r}\frac{\partial \varepsilon_{rr}}{\partial \theta} + 2A_{44}\left(\frac{\partial \varepsilon_{r\theta}}{\partial r} + \frac{3\varepsilon_{r\theta}}{r}\right) = 0,
\end{aligned} \tag{6}$$

where

$$\begin{aligned}
&\varepsilon_1 = \varepsilon_{\theta\theta} + \varepsilon_{\varphi\varphi},\\
&\nabla_1^2 = \frac{\partial^2}{\partial \theta^2} + \cot\theta\frac{\partial}{\partial \theta} + \frac{1}{\sin^2\theta}\frac{\partial^2}{\partial \varphi^2}.
\end{aligned} \tag{7}$$

2.3. Boundary conditions

For the sphere in equilibrium, the ith load of magnitude F_i is applied on the ith circular load area A_i, which subtends an angle of $2\phi_i$ from the center of the sphere as shown in Fig. 3. It is assumed that the load is axisymmetrically distributed in each load area. The symmetry axis, namely loading axis, is the line across the center of the load area (R, θ_i, φ_i) and the sphere center. The position of the ith load is denoted by (θ_i, φ_i) in the remainder of this paper. The pressure p_i is distributed along the radial direction in the range of $0 \leqslant \phi \leqslant \phi_i$. Subsequently, the boundary conditions can be written as

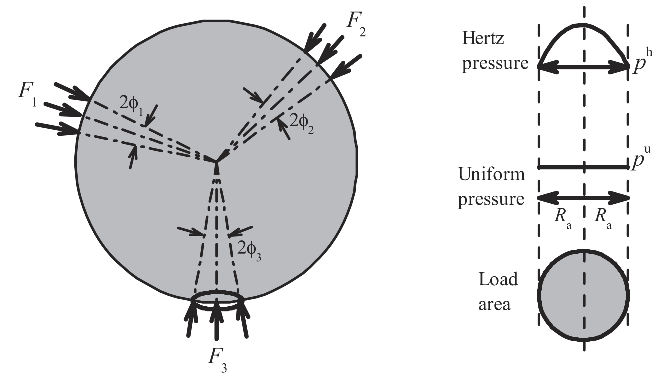

Fig. 3. Left: sketch of a special load configuration where the centers of three load areas lie on the same plane; right: two different choices of pressure distribution.

$$\sigma_{rr}^i(\phi) = \begin{cases} p_i(\phi) & 0 \leqslant \phi \leqslant \phi_i, \\ 0 & \text{in the other areas} \end{cases} \tag{8}$$

and

$$\sigma_{r\varphi} = \sigma_{r\theta} = 0, \tag{9}$$

on $r = R$, where R is the radius of sphere. p_i is a pressure distribution which can be any kind of distribution in this work. In practice, the pressure distribution is induced by contact, e.g., contact between a plate and a sphere. The solution obtained in this work allows for adopting such pressure distributions giving rise to the same stress state in the sphere as that induced in a real contact. In order to obtain an explicit pressure distribution, its distribution form and the relation between pressure amplitude and resultant load have to be assumed. The relevance of our solution in relation to, say, the experiment depends on the choice of a realistic pressure distribution in the above sense.

Two pressure distributions, i.e., uniform pressure p^{u} and Hertz pressure p^{h}, are considered

$$p_i^{\mathrm{u}}(\phi) = -p_{\mathrm{u}}, \tag{10}$$

$$p_i^{\mathrm{h}}(\phi) = -p_{\max}\left[1 - \left(\frac{\sin\phi}{\sin\phi_i}\right)^2\right]^{\frac{1}{2}}, \tag{11}$$

where p_{u} is the uniform pressure and $p_{\max}$ is the maximum pressure in the load area. Both of them are determined by the relation between pressure and load. The Hertz pressure distribution in Eq. (11) conforms to the Hertz pressure expression of Eq. (3.39) in Johnson (1987) for isotropic material under smooth contact. It would represent an approximation for a material having spherically isotropic elasticity.

For the uniform pressure, the relation

$$\int_{A_i} p_i\, dA = \int_0^{\phi_i} p_i 2\pi R^2 \sin\phi\, d\phi = -F_i, \tag{12}$$

has been used by Hiramatsu and Oka (1966) and Chau and Wei (1999) to derive the analytical solutions for stresses in a sphere subjected to a pair of diametral loads (for the case of $R_{a1} = R_{a2}$ in Fig. 4). Here, A is the initial surface load area. The pressure is applied on the initial (undeformed) load area as shown in Fig. 4. The uniform pressure reads as

$$p_{\mathrm{u}} = \frac{F_i}{2\pi R^2(1 - \cos\phi_i)}. \tag{13}$$

Substitution of Eq. (11) into (12) yields

$$p_{\max} = \frac{F_i}{\pi R^2}\frac{1}{1 - \operatorname{arctanh}(\sin\phi_i)\cot\phi_i\cos\phi_i}. \tag{14}$$

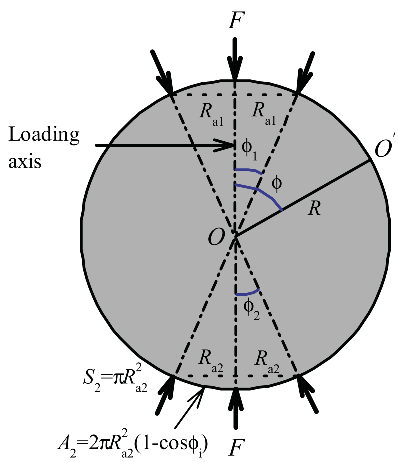

Fig. 4. Diametral loading on a sphere. R_{a1} and R_{a2} are two load radii. O' is a point on the surface. ϕ ranging from 0 to $\pi/2$ is the angle between the loading axis and the line across O and O'.

Both pressure distributions, uniform and Hertz, will be used in our analysis. The uniform distribution, namely Eqs. (10) and (13), will be used to validate the solution obtained in this work by comparison with the results calculated by Chau and Wei (1999). The Hertz distribution, namely Eqs. (11) and (14), should be closer to the one in an elastic contact. Thus, Hertz pressure is better than uniform pressure to represent the case for elastic contact.

For the Hertz pressure distribution, another relation between pressure and load reads as

$$\int_{S_i} p_i\, dS = \int_0^{\phi_i} p_i 4\pi R^2 \sin\phi\cos\phi\, d\phi = -F_i, \tag{15}$$

where S is the area of the load circle with a radius R_a. The pressure is applied on the circular area along the load axis direction. The derived $p_{\max}$ is exactly the one derived by Hertz (1881) as

$$p_{\max} = \frac{3}{2}\frac{F_i}{\pi R_a^2} = \frac{F_i}{2\pi R^2}\frac{3}{\sin^2\phi_i}. \tag{16}$$

The Hertz distribution together with Eq. (16) was used by Chau et al. (2000) for the case of a pair of rigid plates compressing an elastic sphere. However, the value $p_{\max}$ calculated from Eqs. (14) and (16), respectively, differ by a small amount. For example, the difference is less than 0.2% for the same F_i, R and $\phi_i = 5°$, which means the corresponding stress difference at any point in the sphere will be less than 0.2%. Accordingly, the $p_{\max}$ in Eq. (14) is used in this work.

Force equilibrium requires that

$$\begin{aligned} &\sum_i F_i \cos\theta_i = 0, \\ &\sum_i F_i \sin\theta_i \cos\varphi_i = 0, \\ &\sum_i F_i \sin\theta_i \sin\varphi_i = 0. \end{aligned} \tag{17}$$

2.4. Displacement functions

It was proposed by Hu (1954) that the displacements under consideration can be expressed by two displacement potential functions. In order to get the explicit roots for the governing equations, Chau and Wei (1999) have made some changes of the variables introduced by Ding and Ren (1991). As a result, two displacement potentials Z and Φ are derived, which satisfy

$$A_{44}\left(\frac{\partial^2 Z}{\partial\eta^2} + \frac{\partial Z}{\partial\eta}\right) + A_{66}\nabla_1^2 Z - 2(A_{44} - A_{66})Z = 0, \tag{18}$$

$$\left[\begin{array}{c}\left(\frac{\partial^2}{\partial\eta^2} + \frac{\partial}{\partial\eta}\right)^2 + 2D\left(\frac{\partial^2}{\partial\eta^2} + \frac{\partial}{\partial\eta}\right) + M\nabla_1^2\left(\frac{\partial^2}{\partial\eta^2} + \frac{\partial}{\partial\eta}\right) \\ -4L + 2(N-L)\nabla_1^2 + N\nabla_1^2\nabla_1^2\end{array}\right]\Phi = 0. \tag{19}$$

Appendix A shows the details including the introduced variables, such as Z, F, H and η, and parameters, such as D, L, M and N. The displacement components read as

$$\begin{aligned} u_\theta &= -\frac{1}{\sin\theta}\frac{\partial Z}{\partial\varphi} + \left[d\frac{\partial}{\partial\eta} + 2(a+b)\right]\frac{\partial\Phi}{\partial\theta}, \\ u_\varphi &= \frac{\partial Z}{\partial\theta} + \frac{1}{\sin\theta}\left[d\frac{\partial}{\partial\eta} + 2(a+b)\right]\frac{\partial\Phi}{\partial\phi}, \\ u_r &= -\left[h\left(\frac{\partial^2}{\partial\eta^2} + \frac{\partial}{\partial\eta}\right) + a\nabla_1^2 - 2b\right]\Phi. \end{aligned} \tag{20}$$

The strain and stress components can be expressed in terms of Z and Φ by substitution of Eq. (20) into (4) and (1) subsequently. Now it is clear that when Z and Φ are known, the problem is solved.

Inspired by the displacement functions used by Chau and Wei (1999), the solution form

$$Z = \sum_{n=0}^{\infty}\sum_{m=0}^{n} e^{\lambda_n\eta} S_{nm}(\theta,\varphi) \tag{21}$$

is sought for the displacement function Z, where

$$S_{nm}(\theta,\varphi) = (D_{nm}^1 \cos m\varphi + D_{nm}^2 \sin m\varphi)P_n^m(\cos\theta). \tag{22}$$

D_{nm}^1, D_{nm}^2 and λ_n are constants. $P_n^m(x)$ is the associated Legendre function. S_{nm} satisfies

$$\nabla_1^2 S_{nm}(\theta,\varphi) + n(n+1)S_{nm}(\theta,\varphi) = 0. \tag{23}$$

Both n and m are integers. n ranges from 0 to infinity and m ranges from 0 to n. Substitution of Eq. (21) into (18) yields

$$\lambda_n^2 + \lambda_n - M_n = 0, \tag{24}$$

where

$$M_n = 2 + (n-1)(n+2)\frac{A_{66}}{A_{44}}. \tag{25}$$

The two characteristic roots for Eq. (24) are

$$\lambda_{n1} = \frac{-1+\sqrt{1+4M_n}}{2}, \quad \lambda_{n2} = \frac{-1-\sqrt{1+4M_n}}{2}. \tag{26}$$

As a result, if $\lambda_{n1} \neq \lambda_{n2}$, Z reads as

$$\begin{aligned} Z &= \sum_{n=0}^{\infty}\sum_{m=0}^{n}\left(D_{n1}^m e^{\lambda_{n1}\eta} + D_{n3}^m e^{\lambda_{n2}\eta}\right)\cos m\varphi P_n^m(\cos\theta) \\ &\quad + \sum_{n=0}^{\infty}\sum_{m=0}^{n}\left(D_{n2}^m e^{\lambda_{n1}\eta} + D_{n4}^m e^{\lambda_{n2}\eta}\right)\sin m\varphi P_n^m(\cos\theta), \end{aligned} \tag{27}$$

where D_{ni}^m $(i = 1,2,3,4)$ are unknown coefficients. Similarly, the solution form

$$\Phi = \sum_{n=0}^{\infty}\sum_{m=0}^{n} e^{\mu_n\eta} S'_{nm}(\theta,\varphi) \tag{28}$$

is sought for the displacement function Φ, where

$$S'_{nm}(\theta,\varphi) = (C_{nm}^1 \cos m\varphi + C_{nm}^2 \sin m\varphi)P_n^m(\cos\theta). \tag{29}$$

Substitution of Eq. (28) into Eq. (19) yields

$$(\mu_n^2 + \mu_n)^2 + 2P_n(\mu_n^2 + \mu_n) + Q_n = 0, \tag{30}$$

where

$$P_n = D - n(n+1)\frac{M}{2}, \quad Q_n = (n+2)(n-1)[2L + n(n+1)N]. \tag{31}$$

The four characteristic roots for Eq. (30) are

$$\mu_{n1} = \frac{-1+\sqrt{\varsigma_n}}{2}, \quad \mu_{n2} = \frac{-1+\sqrt{\xi_n}}{2}, \quad \mu_{n3} = \frac{-1-\sqrt{\varsigma_n}}{2},$$
$$\mu_{n4} = \frac{-1-\sqrt{\xi_n}}{2}, \tag{32}$$

where

$$\varsigma_n = 1 - 4\left(P_n + \sqrt{P_n^2 - Q_n}\right), \quad \xi_n = 1 - 4\left(P_n - \sqrt{P_n^2 - Q_n}\right). \tag{33}$$

If these roots are distinct, Φ reads as

$$\begin{aligned}\Phi = & \sum_{n=0}^{\infty}\sum_{m=0}^{n}\left(C_{n1}^m e^{\mu_{n1}\eta} + C_{n2}^m e^{\mu_{n2}\eta} + C_{n5}^m e^{\mu_{n3}\eta} + C_{n6}^m e^{\mu_{n4}\eta}\right)\cos m\varphi P_n^m(\cos\theta) \\ & + \sum_{n=0}^{\infty}\sum_{m=0}^{n}\left(C_{n3}^m e^{\mu_{n1}\eta} + C_{n4}^m e^{\mu_{n2}\eta} + C_{n7}^m e^{\mu_{n3}\eta} + C_{n8}^m e^{\mu_{n4}\eta}\right)\sin m\varphi P_n^m(\cos\theta),\end{aligned} \tag{34}$$

where C_{ni}^m $(i = 1, 2, \ldots, 8)$ are unknown coefficients. The proposed Z and Φ depend on φ, which enables to resolve the solution for asymmetric boundary conditions. For example, when a sphere is subjected to three loads along different directions, the load boundary condition is asymmetric.

2.5. Characteristic roots

Chau and Wei (1999) concluded that all roots for λ_n and μ_n with a real part less than 1 would lead to infinite stresses at the sphere center and have to be discarded. Furthermore, the analysis also indicated that the real parts of λ_{n2}, μ_{n3} and μ_{n4} are less than 1. Consequently, D_{n3}^m, D_{n4}^m, and C_{ni}^m $(i = 5, 6, 7, 8)$ should be set to zero. As a result, Eq. (27) reduces to

$$Z = \sum_{n=0}^{\infty}\sum_{m=0}^{n}\left[D_{n1}^m e^{\lambda_{n1}\eta}\cos m\varphi P_n^m(\cos\theta) + D_{n2}^m e^{\lambda_{n1}\eta}\sin m\varphi P_n^m(\cos\theta)\right]. \tag{35}$$

On the other hand, there are two cases for Φ.

Case I: Two real roots

If $P_n^2 - Q_n > 0$, $\xi_n > 0$ and $\varsigma_n > 0$, μ_{n1} and μ_{n2} are two real unequal roots. If $\mu_{n1} \geqslant 1$ and $\mu_{n2} \geqslant 1$, the resultant solution is

$$\begin{aligned}\Phi_n^m = & \left(C_{n1}^m e^{\mu_{n1}\eta} + C_{n2}^m e^{\mu_{n2}\eta}\right)\cos m\varphi P_n^m(\cos\theta) \\ & + \left(C_{n3}^m e^{\mu_{n1}\eta} + C_{n4}^m e^{\mu_{n2}\eta}\right)\sin m\varphi P_n^m(\cos\theta).\end{aligned} \tag{36}$$

If $\mu_{n1} < 1$ and $\mu_{n2} < 1$, there are no converging solutions.

Case II: Two complex conjugate roots

If $P_n^2 - Q_n < 0$, μ_{n1} and μ_{n2} are two complex conjugates. If the real part for both μ_{n1} and μ_{n2} is not less than 1, the resultant solution is

$$\begin{aligned}\Phi_n^m = & \left(E_{n1}^m e^{\mu_n\eta} + \bar{E}_{n1}^m e^{\bar{\mu}_n\eta}\right)\cos m\varphi P_n^m(\cos\theta) \\ & + \left(E_{n2}^m e^{\mu_n\eta} + \bar{E}_{n2}^m e^{\bar{\mu}_n\eta}\right)\sin m\varphi P_n^m(\cos\theta),\end{aligned} \tag{37}$$

where $E_{n\alpha}^m = R_{n\alpha}^m + iI_{n\alpha}^m (\alpha = 1, 2)$ are complex constants and $\mu_n = x_n + iy_n$ with

$$x_n + iy_n = \frac{-1 + \sqrt{1 - 4P_n - i4\sqrt{|P_n^2 - Q_n|}}}{2}. \tag{38}$$

$\bar{E}_{n\alpha}^m$ and $\bar{\mu}_n$ are complex conjugates of $E_{n\alpha}^m$ and μ_n, respectively.

Subsequently, the general solution for Φ is

$$\Phi = \sum_{n=0}^{\infty}\sum_{m=0}^{n}\Phi_n^m, \tag{39}$$

where Φ_n^m is defined either in Eq. (36) or (37), which depends on the type of μ_n.

2.6. The general solution

Substituting Eqs. (35) and (39) into Eqs. (20), (4) and (1) subsequently, the stress components read as

$$\begin{aligned}\sigma_{\theta\theta} = & -\frac{1}{R}\sum_{h=0}^{\infty}\sum_{i=1}^{2}\sum_{m=0}^{h}D_{hi}^m\rho^{\lambda_{hi}-1} \\ & \times\left\{2A_{66}\csc\theta(-1)^i m\left[\frac{\partial P_h^m(\cos\theta)}{\partial\theta} - \cot\theta P_h^m(\cos\theta)\right]s_i\right\} \\ & -\frac{1}{R}\sum_{l}\sum_{j=1}^{4}\sum_{m=0}^{l}C_{lj}^m\rho^{\mu_{lj}-1}\left\{\begin{array}{l}\left[\begin{array}{c}A_{12}l(l+1)\Gamma_{lj} \\ +(A_{13}\mu_{lj} + 2A_{12} + 2A_{66})\Lambda_{lj}\end{array}\right]P_l^m(\cos\theta) \\ -2A_{66}\Gamma_{lj}\frac{\partial^2 P_l^m(\cos\theta)}{\partial\theta^2}\end{array}\right\}cs_j \\ & +\frac{1}{R}\sum_{n}\sum_{k=1}^{2}\sum_{m=0}^{n}\rho^{x_n-1}\left\{\begin{array}{l}\left[\begin{array}{l}\Omega_1(R_{nk}^m, I_{nk}^m)\cos(y_n\ln\rho) \\ +\Omega_1(-I_{nk}^m, R_{nk}^m)\sin(y_n\ln\rho)\end{array}\right]P_n^m(\cos\theta) \\ -\left[\begin{array}{l}\Omega_2(R_{nk}^m, I_{nk}^m)\cos(y_n\ln\rho) \\ +\Omega_2(-I_{nk}^m, R_{nk}^m)\sin(y_n\ln\rho)\end{array}\right]\frac{\partial^2 P_n^m(\cos\theta)}{\partial\theta^2}\end{array}\right\}sc_k,\end{aligned} \tag{40}$$

$$\begin{aligned}\sigma_{r\varphi} = & \frac{1}{R}\sum_{h=0}^{\infty}\sum_{i=1}^{2}\sum_{m=0}^{h}D_{hi}^m\rho^{\lambda_{hi}-1}(\lambda_{hi} - 1)\frac{\partial P_h^m(\cos\theta)}{\partial\theta}sc_i \\ & -\frac{\csc\theta}{R}\sum_{l}\sum_{j=1}^{4}\sum_{m=0}^{l}\left\{A_{44}C_{lj}^m\rho^{\mu_{lj}-1}\left[(1-\mu_{lj})\Gamma_{lj} + \Lambda_{lj}\right]\right\} \\ & \times sgn_j P_l^m(\cos\theta)cs_{5-j} + \frac{\csc\theta}{R}\sum_{n}\sum_{k=1}^{2}\sum_{m=0}^{n}\rho^{x_n-1} \\ & \times\left[\begin{array}{l}\Pi(R_{nk}^m, I_{nk}^m)\cos(y_n\ln\rho) \\ +\Pi(-I_{nk}^m, R_{nk}^m)\sin(y_n\ln\rho)\end{array}\right](-1)^k m P_n^m(\cos\theta)s_k,\end{aligned} \tag{41}$$

$$\begin{aligned}\sigma_{r\theta} = & -\frac{\csc\theta}{R}\sum_{h=0}^{\infty}\sum_{i=1}^{2}\sum_{m=0}^{h}D_{hi}^m\rho^{\lambda_{hi}-1}(\lambda_{hi} - 1)(-1)^i m P_h^m(\cos\theta)s_i \\ & -\frac{1}{R}\sum_{l}\sum_{j=1}^{4}\sum_{m=0}^{l}\left\{A_{44}C_{lj}^m\rho^{\mu_{lj}-1}\left[(1-\mu_{lj})\Gamma_{lj} + \Lambda_{lj}\right]\right\}\frac{\partial P_l^m(\cos\theta)}{\partial\theta}cs_j \\ & +\frac{1}{R}\sum_{n}\sum_{k=1}^{2}\sum_{m=0}^{n}\rho^{x_n-1}\left[\begin{array}{l}\Pi(R_{nk}^m, I_{nk}^m)\cos(y_n\ln\rho) \\ +\Pi(-I_{nk}^m, R_{nk}^m)\sin(y_n\ln\rho)\end{array}\right]\frac{\partial P_n^m(\cos\theta)}{\partial\theta}sc_k,\end{aligned} \tag{42}$$

$$\begin{aligned}\sigma_{\theta\varphi} = & \frac{A_{66}}{R}\sum_{h=0}^{\infty}\sum_{i=1}^{2}\sum_{m=0}^{h}D_{hi}^m\rho^{\lambda_{hi}-1}\left[\frac{\partial^2 P_h^m(\cos\theta)}{\partial\theta^2} - \cot\theta\frac{\partial P_h^m(\cos\theta)}{\partial\theta}\right. \\ & \left.+\frac{m^2}{\sin^2\theta}P_h^m(\cos\theta)\right]sc_i + \frac{2A_{66}}{R\sin\theta}\sum_{l}\sum_{j=1}^{4}\sum_{m=0}^{l}C_{lj}^m\rho^{\mu_{lj}-1}\Gamma_{lj}sgn_j m \\ & \times\left[\frac{\partial P_l^m(\cos\theta)}{\partial\theta} - \cot\theta P_l^m(\cos\theta)\right]cs_{5-j} \\ & +\frac{2A_{66}}{R\sin\theta}\sum_{n}\sum_{k=1}^{2}\sum_{m=0}^{n}\Xi^n(R_{nk}, I_{nk})(-1)^k m \\ & \times\left[\frac{\partial P_n^m(\cos\theta)}{\partial\theta} - \cot\theta P_n^m(\cos\theta)\right]s_k,\end{aligned} \tag{43}$$

where $\rho = r/R$ is the normalized radial coordinate. The notations and functions

$$s_2 = cs_1 = cs_2 = sc_1 = \cos m\varphi, \tag{44a}$$

$$s_1 = cs_3 = cs_4 = sc_2 = \sin m\varphi, \tag{44b}$$

$$sgn_1 = sgn_2 = -sgn_3 = -sgn_4 = -1, \tag{44c}$$

$$\mu_{l3} = \mu_{l1}, \quad \mu_{l4} = \mu_{l2}, \tag{44d}$$

$$\Gamma_{lj} = d\mu_{lj} + 2(a+b), \tag{44e}$$

$$\Lambda_{lj} = h\mu_{lj}(\mu_{lj}+1) - 2b - al(l+1), \tag{44f}$$

$$\begin{aligned}\Omega_1(R,I) = {} & 4A_{44}(A_{12}+A_{66})\left[I(2x_n+1)y_n - R(x_n^2-y_n^2+x_n)\right] \\ & + A_{12}n(n+1)[2d(Iy_n - Rx_n) - 4(a+b)R] \\ & + 2A_{44}A_{13}\left[(Ix_n+Ry_n)(2x_n+1)y_n - (Rx_n - Iy_n)(x_n^2-y_n^2+x_n)\right] \\ & + 2[2b+an(n+1)][2(A_{12}+A_{66})R + A_{13}(Rx_n - Iy_n)],\end{aligned} \tag{44g}$$

$$\Omega_2(R,I) = 2A_{66}[2d(Iy_n - Rx_n) - 4(a+b)R], \tag{44h}$$

$$\begin{aligned}\Pi(R,I) = {} & A_{44}\left\{\begin{array}{c} Iy_n[2d(1-2x_n) - 4(a+b)] \\ +R[2d(x_n^2-y_n^2-x_n) + 4(a+b)(x_n-1)] \end{array}\right\} \\ & - 2A_{44}^2\left[R(x_n^2-y_n^2+x_n) - I(2x_n+1)y_n\right] \\ & + 2A_{44}[2b+an(n+1)]R,\end{aligned} \tag{44i}$$

$$\Xi^n(R,I) = 2\rho^{x_n-1}\left\{\begin{array}{l} [R\cos(y_n\ln\rho) - I\sin(y_n\ln\rho)][dx_n + 2(a+b)] \\ -[I\cos(y_n\ln\rho) + R\sin(y_n\ln\rho)]dy_n \end{array}\right\}, \tag{44j}$$

have been used.

The unknown coefficients in the above equations can be obtained by evaluating the boundary conditions, i.e., Eqs. (8) and (9). All stress components can be derived when these coefficients are known. Note that the first summation for l is done for the case of two real roots and the second summation for n is done for the case of two complex roots. The relation

$$\frac{-m^2}{\sin^2\theta}P_n^m(\cos\theta) + \frac{\partial^2 P_n^m(\cos\theta)}{\partial\theta^2} + \cot\theta\frac{\partial P_n^m(\cos\theta)}{\partial\theta} = -n(n+1)P_n^m(\cos\theta), \tag{45}$$

which is a variation of Eq. (23) has been used to derive these stresses, namely Eqs. (40)–(43). Note that there is a special case for $n = 0$. For an isotropic material, it holds $\mu_{n1} = (-1 + |2n-1|)/2$ and $\mu_{n2} = n+1$. Although $\mu_{n1} = 0 < 1$ when $n = 0$, it does *NOT* lead to infinite stresses at the sphere center because $\rho^{\mu_{n1}-1}$ in Eq. (40) is multiplied by a zero value. Therefore, the first term for $n = 0$ in the series should be treated separately. Moreover, for isotropic materials $n = 0$ is the only exception of the root requirement concluded by Chau and Wei (1999). Series terms for $n = 0$ of all stress components are independent of positions in a sphere. The terms of $\sigma_{\theta\theta}$, $\sigma_{\varphi\varphi}$ and σ_{rr} for $n = 0$ are A_0^0 (see Eq. (47) below) while the terms for $\sigma_{r\varphi}$,$\sigma_{r\theta}$ and $\sigma_{\theta\varphi}$ are always 0.

The expression for σ_{rr} can be obtained by replacing A_{12}, $(2A_{66})$ and A_{13}, with A_{13}, 0 and A_{33} in Eq. (40), respectively. Replacing A_{12} and $(2A_{66})$ in Eq. (40) by $(2A_{66} + A_{12})$ and $(-2A_{66})$, respectively, yields the expression for $\sigma_{\varphi\varphi}$.

2.7. Determination of unknown coefficients

The union of all loads $p(\theta,\varphi) = \cup p_i(\phi)$ on a sphere surface can be expanded with the associated Legendre function (see Appendix B).

$$p(\theta,\varphi) = \sum_{n=0}^{\infty}\sum_{m=0}^{m=n}(A_n^m\cos m\varphi + B_n^m\sin m\varphi)P_n^m(\cos\theta), \tag{46}$$

where A_n^m and B_n^m are two coefficients determined by

$$\begin{aligned} A_n^m &= \frac{(2n+1)(n-m)!}{2\pi\delta_m(n+m)!}\int_0^{\pi}\int_0^{2\pi}p(\theta,\varphi)P_n^m(\cos\theta)\cos m\varphi\sin\theta\, d\varphi\, d\theta, \\ B_n^m &= \frac{(2n+1)(n-m)!}{2\pi(n+m)!}\int_0^{\pi}\int_0^{2\pi}p(\theta,\varphi)P_n^m(\cos\theta)\sin m\varphi\sin\theta\, d\varphi\, d\theta, \end{aligned} \tag{47}$$

where

$$\delta_m = \begin{cases} 2 & m = 0, \\ 1 & m \neq 0. \end{cases} \tag{48}$$

Consequently, the boundary condition of Eq. (8) becomes

$$\begin{aligned}\sigma_{rr}|_{r=R} &= p(\theta,\varphi) \\ &= \sum_{n=0}^{\infty}\sum_{m=0}^{m=n}(A_n^m\cos m\varphi + B_n^m\sin m\varphi)P_n^m(\cos\theta).\end{aligned} \tag{49}$$

The domain of the integrals in Eq. (47) is shown in Appendix C. Moreover, in Appendix D the angle ϕ as a function of (θ,φ) is derived. In Appendix E the relation between coefficients using the boundary condition of Eq. (9) is obtained. These relations yield the explicit forms of all coefficients in the stress expressions as

$$\begin{aligned} & D_{h1}^m = 0, \quad D_{h2}^m = 0 \\ & C_{l2}^m = -\frac{A_l^m R}{L_{l12}J_{l1} + J_{l2}}, \quad C_{l4}^m = -\frac{B_l^m R}{L_{l12}J_{l1} + J_{l2}}, \\ & R_{n1}^m = \frac{A_n^m R}{H_n}, \quad R_{n2}^m = \frac{B_n^m R}{H_n} \end{aligned} \tag{50}$$

and

$$C_{l1}^m = L_{l12}C_{l2}^m, \quad C_{l3}^m = L_{l12}C_{l4}^m, \quad I_{n1}^m = K_{n12}R_{n1}^m, \quad I_{n2}^m = K_{n12}R_{n2}^m, \tag{51}$$

where

$$J_{lj} = A_{13}l(l+1)\Gamma_{lj} + (A_{33}\mu_{lj} + 2A_{13})\Lambda_{lj}, \tag{52a}$$

$$L_{l12} = -\frac{(1-\mu_{l2})\Gamma_{l2} + \Lambda_{l2}}{(1-\mu_{l1})\Gamma_{l1} + \Lambda_{l1}}, \quad K_{n12} = \frac{\Pi(1,0)}{\Pi(0,-1)}, \tag{52b}$$

$$\begin{aligned} H_n = {} & 4A_{44}A_{13}\left[K_{n12}(2x_n+1)y_n - (x_n^2-y_n^2+x_n)\right] \\ & + A_{13}n(n+1)[2d(K_{n12}y_n - x_n) - 4(a+b)] \\ & + 2A_{44}A_{33}\left[\begin{array}{l}(K_{n12}x_n + y_n)(2x_n+1)y_n \\ -(x_n - K_{n12}y_n)(x_n^2-y_n^2+x_n)\end{array}\right] \\ & + 2[2b+an(n+1)][2A_{13} + A_{33}(x_n - K_{n12}y_n)]. \end{aligned} \tag{52c}$$

2.8. Final solution

Substitution of Eqs. (50) and (51) into (40)–(43) gives the final expressions for stress components as

$$\begin{aligned}\sigma_{\theta\theta} = {} & \sum_l\sum_{m=0}^{l}\left[\frac{A_l^m}{L_{l12}J_{l1}+J_{l2}}\cos m\varphi + \frac{B_l^m}{L_{l12}J_{l1}+J_{l2}}\sin m\varphi\right]\Theta_l \\ & + \sum_n\sum_{m=0}^{n}\left[\frac{A_n^m}{H_n}\cos m\varphi + \frac{B_n^m}{H_n}\sin m\varphi\right]\Theta_n,\end{aligned} \tag{53}$$

$$\begin{aligned}\sigma_{r\varphi} = {} & \sum_l\sum_{m=0}^{l}\Xi_l\left[-\frac{A_l^m}{L_{l12}J_{l1}+J_{l2}}\sin m\varphi + \frac{B_l^m}{L_{l12}J_{l1}+J_{l2}}\cos m\varphi\right] \\ & \times m\csc\theta P_l^m(\cos\theta) + \sum_n\sum_{m=0}^{n}\Xi_n\left[-\frac{A_n^m}{H_n}\sin m\varphi + \frac{B_n^m}{H_n}\cos m\varphi\right] \\ & \times m\csc\theta P_n^m(\cos\theta),\end{aligned} \tag{54}$$

$$\sigma_{r\theta} = \sum_l \sum_{m=0}^{l} \Xi_l \left[\frac{A_l^m}{L_{l12}J_{l1} + J_{l2}} \cos m\varphi + \frac{B_l^m}{L_{l12}J_{l1} + J_{l2}} \sin m\varphi \right] \times \frac{\partial P_l^m(\cos\theta)}{\partial\theta} + \sum_n \sum_{m=0}^{n} \Xi_n \left[\frac{A_n^m}{H_n} \cos m\varphi + \frac{B_n^m}{H_n} \sin m\varphi \right] \frac{\partial P_n^m(\cos\theta)}{\partial\theta}, \quad (55)$$

$$\sigma_{\theta\varphi} = \left\{ \begin{array}{l} \sum\limits_l \sum\limits_{m=0}^{l} \Xi^l \left[\frac{A_l^m}{L_{l12}J_{l1}+J_{l2}} \sin m\varphi - \frac{B_l^m}{L_{l12}J_{l1}+J_{l2}} \cos m\varphi \right], \\ \sum\limits_n \sum\limits_{m=0}^{n} \Xi^n(1, K_{n12}) \left[-\frac{A_n^m}{H_n} \sin m\varphi + \frac{B_n^m}{H_n} \cos m\varphi \right] \end{array} \right\} \times \frac{2mA_{66}}{\sin\theta} \left[\frac{\partial P_i^m(\cos\theta)}{\partial\theta} - \cot\theta P_i^m(\cos\theta) \right] \quad (i = l \text{ or } n), \quad (56)$$

where

$$\Theta_l = \sum_{j=1}^{2} \delta_{lj} \rho^{\mu_{lj}-1} \left\{ \begin{array}{l} \left[A_{12} l(l+1) \Gamma_{lj} + (A_{13}\mu_{lj} + 2A_{12} + 2A_{66}) \Lambda_{lj} \right] \\ \times P_l^m(\cos\theta) - 2A_{66} \Gamma_{lj} \frac{\partial^2 P_l^m(\cos\theta)}{\partial\theta^2} \end{array} \right\}, \quad (57a)$$

$$\Theta_n = \rho^{x_n - 1} \left\{ \begin{array}{l} \left[\begin{array}{l} \Omega_1(1, K_{n12}) \cos(y_n \ln\rho) \\ +\Omega_1(-K_{n12}, 1) \sin(y_n \ln\rho) \end{array} \right] P_n^m(\cos\theta) \\ -\left[\begin{array}{l} \Omega_2(1, K_{n12}) \cos(y_n \ln\rho) \\ +\Omega_2(-K_{n12}, 1) \sin(y_n \ln\rho) \end{array} \right] \frac{\partial^2 P_l^m(\cos\theta)}{\partial\theta^2} \end{array} \right\}, \quad (57b)$$

$$\Xi_l = \sum_{j=1}^{2} \delta_{lj} A_{44} \rho^{\mu_{lj}-1} \left[(1 - \mu_{lj}) \Gamma_{lj} + \Lambda_{lj} \right] \quad (57c)$$

$$\Xi_n = \rho^{x_n - 1} [\Pi(1, K_{n12}) \cos(y_n \ln\rho) + \Pi(-K_{n12}, 1) \sin(y_n \ln\rho)], \quad (57d)$$

$$\Xi^l = L_{l12} \rho^{\mu_{l1}-1} \Gamma_{l1} + \rho^{\mu_{l2}-1} \Gamma_{l2}, \quad (57e)$$

$$\delta_{lj} = \begin{cases} L_{l12} & j = 1, \\ 1 & j = 2. \end{cases} \quad (57f)$$

The expression for σ_{rr} can be obtained by replacing A_{12}, $(2A_{66})$ and A_{13}, with A_{13}, 0 and A_{33} in Eq. (53). Replacing A_{12} and $(2A_{66})$ in Eq. (53) by $(2A_{66} + A_{12})$ and $(-2A_{66})$, respectively, yields the expression for $\sigma_{\varphi\varphi}$. Note that for both cases, σ_{rr} and $\sigma_{\varphi\varphi}$, Eqs. (52) remain unchanged.

3. Numerical evaluation and discussion

In view of the application to pebbles, we will report mainly the numerical evaluation for isotropic materials. Nevertheless, we will also present some cases with spherical isotropy. As stated in Section 2.6, it holds that $\mu_{n1} = (-1 + |2n - 1|)/2$ and $\mu_{n2} = n + 1$ for an isotropic material. The roots are two unequal real numbers which are not less than 1 for $n \geqslant 2$. Thus, there are only $l = 0, 2, 3, \ldots, \infty$ terms for the case of two real roots in the analytical solution obtained in this work, namely Eqs. (53)–(56). The term for $l = 1$ is discarded because of the root requirement (see Section 2.5). The analytical solution is evaluated numerically by summing a finite number of terms. N_t is defined as the number of summing terms which are not equal to zero. Hiramatsu and Oka (1966) derived the analytical solution for an isotropic sphere subjected to a pair of diametral loads (for the case of $R_{a1} = R_{a2}$ in Fig. 4). As for that solution, Wijk (1978) indicated that no good convergence can be achieved if the number of summing terms N_t is less than 20. The convergence rate of our solution will be discussed in the next section. Chau and Wei (1999) derived the corresponding solution for a spherically isotropic sphere. Uniform pressure was used in both analyses. However, the well-known Hertz pressure distribution should be applied if the loads are induced by elastic contacts. It is expected that different pressure distributions should have influence only on regions not far from the load area, and have little influence on the sphere center. In the crush tests with elastic plates, the radius of the load area R_a can be measured or calculated for different plates. The input parameter ϕ_i in Eq. (11) corresponds to this radius. The relation between these quantities is $R_a = R\sin\phi_i$. Hence, our solution for Hertz pressure should represent the experimental situation when the two radii of the opposite load areas are the same.

3.1. Validation of the solution for diametral loads: $N_c = 2$

Analytical solutions for stresses in a sphere subjected to diametral loads, namely $N_c = 2$, have been derived by Hiramatsu and Oka (1966) and Chau and Wei (1999) for isotropic and spherically isotropic materials, respectively. Let the principal stresses be denoted by $\sigma_1 \geqslant \sigma_2 \geqslant \sigma_3$, respectively. Applying Eq. (11) to the solution derived by Chau and Wei (1999) the influence of pressure distributions is shown in Fig. 5. The principal stresses along the loading axis are plotted for both pressure distributions, uniform and Hertz pressure. The result for $\phi_i = 5°$ and $\nu = 0.1$ has been demonstrated by Chau and Wei (1999) for the uniform pressure distribution. A relatively small Poisson's ratio $\nu = 0.1$ is used in Fig. 5, so that the influence of pressure distributions can be distinctly illustrated. Note that tensile stresses are positive and compressive stresses are negative. Besides, it holds $\sigma_2 = \sigma_1$ along the loading axis for both pressure distributions. The maximum principal stress at $\rho \approx 0.85$ for Hertz pressure becomes higher than for uniform pressure. The minimum principal stress is hardly influenced by the pressure distribution. Moreover, the pressure distribution has little influence on stresses near the center of the sphere, as expected. The curves in Fig. 5 can be used to validate the solution derived in this work.

Fig. 6 shows the numerical evaluation for our solution for the same case as studied by Hiramatsu and Oka (1966) and Chau and Wei (1999). The loads lie in $(60°, 36°)$ and $(120°, 216°)$ (coordinates explained in Section 2.3), respectively. Both load areas correspond to $\phi_i = 5°$. Note that in our solution loads cannot lie near $\theta = 0$ and $\theta = \pi$ (see Appendix C). The numerical evaluations have been truncated at $N_t = 25$. It should be noted that the terms with odd number of n are zero because of load symmetry. The stresses along the loading axis for $\nu = 0.1$ coincide with those in Fig. 5, which validates our solution. The stresses for $\nu = 0.25$ which is the Poisson's ratio of Li_4SiO_4 pebbles (Vollath et al., 1990) are plotted as well.

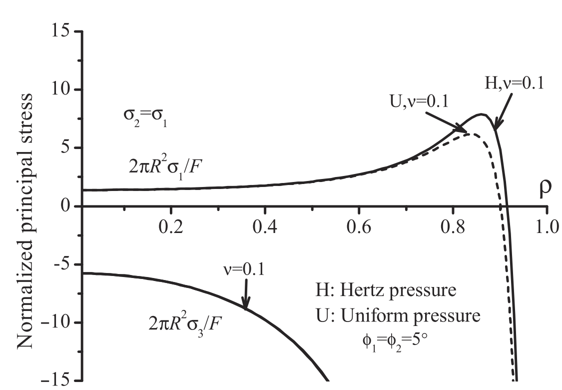

Fig. 5. Normalized principal stress along the loading axis ($\theta = 0°$) calculated from the solution derived by Chau and Wei (1999). In addition, the proposed Hertz pressure distribution, namely Eq. (11), has been implemented into the solution.

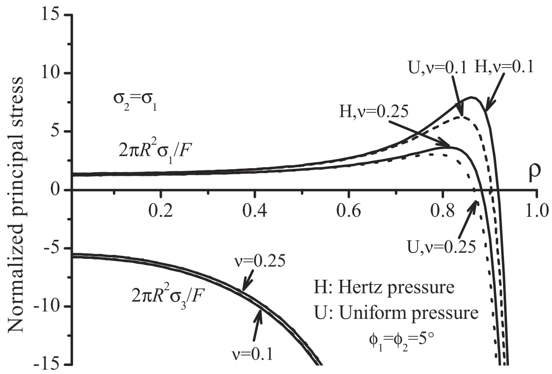

Fig. 6. Normalized principal stress along the loading axis ($\theta = 60°, \varphi = 36°$) calculated from our solution for $N_c = 2$.

The difference between the two pressure distributions becomes smaller when ν increases.

To further validate our analytical solution, FEM simulations have been performed. Table 1 lists the maximum tensile stress and maximum shear stress along the loading axis derived from our solution, FEM simulations and the Hüber–Hertz solution (Hüber, 1904), respectively. Hüber (1904) derived stresses within the Hertzian elastic contact field in a cylindrical coordinate system based on Hertz theory (Hertz, 1881). For the values in this table computed from our solution, the input variables, such as F and ϕ, are the same as those for the Hertz pressure distribution and $\nu = 0.25$ in Fig. 6. The stresses are evaluated with more terms, namely $N_t = 300$, in order to achieve high accuracy. The sphere radius is set to $R = 0.25$ mm corresponding to the mean size of pebbles. Crush tests for Li_4SiO_4 pebbles by BK7 glass plates carried out at Fusion Material Lab (FML) at Karlsruhe Institute of Technology (KIT) are simulated by the finite element method. Young's modulus and Poisson's ratio of BK7 glass is 82 GPa and 0.206, respectively. The spherical pebbles have a radius $R = 0.25$ mm, and interface friction is not taken into account. A Young's modulus of 90 GPa for Li_4SiO_4 pebbles as used by Gan and Kamlah (2010), $\phi_i = 5°$ corresponds to a load of $F = 2.497$ N according to the Hertz theory. For the convenience of comparison, $F = 2.497$ N is used to calculate the stresses in each method. It is relevant to mention that the mesh size along the loading axis is 0.125 μm. A single contact between a sphere and a plate is considered in the Hüber–Hertz solution. Material parameters and the contact load are the same as those used in the FEM simulation. The set of parameters for each method corresponds to the same load case. Therefore, the results are comparable for such a small load.

The maximum tensile stress from Hüber–Hertz solution lies a little closer to the load area than the other methods. All σ_{max} in Table 1 appear nearly at the same location. The relative difference between them is less than 3%. On the other hand, the maximum shear stresses appear almost at the same position close to the load area with a relative difference of less than 1.5%. This good agreement validates our analytical solution and shows its applicability even near the load area. Note that the stresses in the sphere depend on the pair of loads in FEM simulations and our solution. They only depend on a single contact load for the Hüber–Hertz solution. Accordingly, there could be a difference to some extent. For example, $\sigma_{max} \approx 1.6$ MPa at the sphere center according to the Hüber–Hertz solution while $\sigma_{max} \approx 7.9$ MPa according to the FEM simulation and our solution. This difference indicates the invalidity of applying Hüber–Hertz solution at points away from the load area.

Table 1
Maximum tensile tress σ_{max} and shear stress τ_{max} along the loading axis.

	Position: σ_{max} (MPa)	Position: τ_{max} (MPa)
Our solution	$\rho = 0.811$:23.2	$\rho = 0.955$:797
FEM simulation	$\rho = 0.812$:23.8	$\rho = 0.956$:801
Hüber–Hertz solution	$\rho = 0.825$:22.9	$\rho = 0.957$:808

3.2. Evaluation by our solution for general load scenarios: $N_c > 2$

Our solution enables the stress analysis for a sphere subjected to various loads, i.e., $N_c > 2$. Fig. 7 shows the principal stresses along one loading axis for $\nu = 0.25$ subjected to 6 Hertz pressures, i.e., $N_c = 6$. The stresses are evaluated with $N_t = 25$. The loads lie in (60°,36°), (120°,216°), (90°,126°), (90°,306°), (150°,36°), (30°,216°), respectively. In this way, they are arranged as three diametrical pairs orthogonal to each other. Besides, the result for $N_c = 2$, $\nu = 0.25$ and Hertz pressure from Fig. 6 is also plotted for comparison. The same load F is applied on each load area with the same size in both cases. In any case, the loads have to satisfy Eq. (17). Compared to the case for $N_c = 2$ the maximum principal stress for $N_c = 6$ change significantly when ρ approaches zero. Tensile stresses become compressive at the sphere center. Note that the relation $\sigma_2 = \sigma_1$ holds for both cases under consideration, namely $N_c = 2$ and $N_c = 6$, and the peak value of σ_1 is also the maximum tensile stress *inside* the whole sphere (the tensile stress on the surface is not taken into account). On the other hand, the stresses stay approximately the same for both cases for $\rho > 0.8$.

The stresses along one loading axis for $N_c = 4$ are shown in Fig. 8. The stresses in this case are also evaluated with $N_t = 25$. The loads lie in (60°,36°), (120°,216°), (90°,126°), (90°,306°), respectively. They are two diametrical pairs orthogonal to each other. Compared to the case $N_c = 2$, the maximum principal stress has increased significantly for a radius $\rho < 0.85$. Its peak value which is the maximum tensile stress inside the sphere increases nearly by 25%. It is thus essential to consider the influence of the coordination number N_c if the tensile stress inside a sphere is of big concern. Similar to Fig. 7, the stresses close to the load area, that is, above a certain value of ρ, are not influenced by N_c. The critical value of ρ which is approximately 0.9 in this case depends on the contact area and Poisson's ratio. The stresses at points that are close to the load area are still dominated by Hertz theory.

3.3. Evaluation for spherically isotropic spheres

The practical significance of our solution lies in the application to the computation of stress fields in isotropic pebbles in pebble beds. On the other hand, since our analytical solution also applies to a spherically isotropic material, we consider this more general

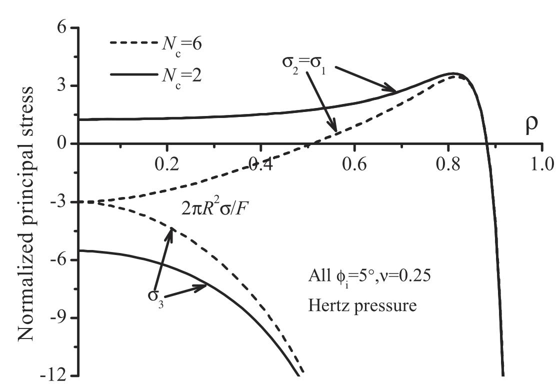

Fig. 7. Normalized principal stress along the loading axis ($\theta = 60°, \varphi = 36°$) calculated from our solution for $N_c = 2$ and $N_c = 6$ for Hertz pressure.

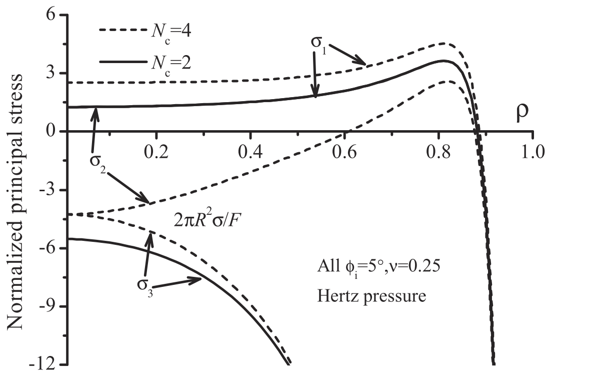

Fig. 8. Normalized principal stress along the loading axis ($\theta = 60°, \varphi = 36°$) calculated from our solution for $N_c = 2$ and $N_c = 4$ for Hertz pressure.

case in the following. Three parameters indicating the degree of anisotropy are defined in agreement to Chau and Wei (1999):

$$\beta = \frac{E}{E'}, \quad \alpha = \frac{\nu'}{\nu}, \quad \xi = \frac{A_{44}}{A_{66}}. \tag{58}$$

Fig. 9 shows the principal stresses along the loading axis for the configuration used for Fig. 8 in the case of $N_c = 4$. There are four cases included in this evaluation: (i) $\beta = 0.95$, $\alpha = 1.0$, $\xi = 1.0$; (ii) $\beta = 1.05$, $\alpha = 1.0$, $\xi = 1.0$; (iii) $\beta = 1.0$, $\alpha = 0.95$, $\xi = 1.0$ and (iv) $\beta = 1.0$, $\alpha = 1.05$, $\xi = 1.0$. Fig. 9 (1) shows the variation of the stress distribution due to a small perturbation of β while Fig. 9 (2) demonstrates the influence of α. The case of $\beta > 1$ means a sphere with a higher stiffness in the spherical hypersurface of isotropy than along the direction perpendicular to the plane, i.e., the radial direction. As for the case $\beta = 1.05$ shown in Fig. 9 (1), all principal stresses stay almost the same compared to those for isotropic material in Fig. 8 except that the magnitude of all stresses in the region near the sphere center decreases slightly in contrast to the isotropic material. On the other hand, when $\beta < 1$, e.g., $\beta = 0.95$, holds, the first principal stress in the range of $0 < \rho < 0.85$ increases significantly compared to the isotropic material, and the second principal stress also increases to some extent in this region. The minimum principal stress increases as well but only around the sphere center, i.e., for $\rho < 0.4$. As to the influence of α on principal stresses, $\alpha < 1$, e.g., $\alpha = 0.95$, hardly has any influence on the stresses inside the whole sphere. On the other hand, $\alpha > 1$, e.g., $\alpha = 1.05$, has a similar influence on the stresses as $\beta = 0.95$ as stated before. It should be noted that small changes for both α and β have no influence on the principal stresses in the region close to the contact area, e.g., $\rho > 0.85$ in both figures.

3.4. Discussion

Our solution has been validated in two ways. First, the three cases studied in Figs. 7–9 have additionally been considered by applying the method of superposition to the solution of Chau and Wei (1999). For this purpose, the load distribution according to Eq. (11) had to be implemented in this solution. Second, the two cases according to Figs. 7 and 8 have been validated by FEM simulation as well. It should be noted that our solution can solve problems for any multiple loads, irrespective of whether these loads have symmetry properties or not. In particular, various sets of equilibrium loads can be applied to a sphere and the stresses in the sphere can subsequently be evaluated. It turns out that stresses in a sphere depend not only on N_c but also load positions. Thus, the conclusion which can be drawn from Figs. 7 and 8 is that N_c does have an influence on the stress field in the sphere. As another feature, our solution accounts for the possibility that the load area can be different even for the same resultant load. For instance, $R_{a1} \neq R_{a2}$ in Fig. 4 can represent the load case that a sphere is compressed by two parallel plates with different stiffnesses.

As mentioned in Section 2.3, the relevance of our solution depends on the consistency between the assumed pressure distribution and the real pressure distribution in the contact zone. The adopted Hertz pressure distribution, namely Eq. (11), and the pressure-load relation, namely Eq. (12), can represent the elastic contact case well for isotropic material according to the results in Table 1. Nevertheless, other pressure distributions correspond to other contact cases. For example, if an elastic sphere is compressed by soft metals, plasticity may occur in the metal. For such a case, if the contact pressure distribution can be derived, such as from FEM simulation, it is expected that the results from our solution with the derived pressure distribution are close to the real case.

There are some technical tips for the numerical evaluation. First, it can be proven that $\Lambda_{01} \equiv 0$ for $l = 0$ in Eq. (44f) holds, independent of material parameters. This causes an exception for $l = 0$ to the root requirement, i.e., all roots μ must be not smaller than 1 (see Section 2.5). In other words, even if $\mu_{01} < 1$ holds stresses at the sphere center are not infinite because Θ_0 in Eq. (57a) is a finite value for $\rho = 0$ as a consequence of $\Lambda_{01} \equiv 0$, provided that $\mu_{02} \geqslant 1$. Thus, the stress term for $l = 0$ in Eq. (53) has to be added in the summation of the stress series although the root μ_{01} is often smaller than 1 which does not satisfy the root requirement as stated before. Second, for the stress term for $l = 1$ in Eq. (53) L_{l12} in Eq. (52b) is often infinite because the denominator is zero as a result of $\mu_{11} = 0$ (see Eq. (32) where P_1 is sometimes negative which depends on material parameters). Under this circumstance, both C_{11} and C_{12} can be set to zero such that Eq. (E.9) in Appendix E can be satisfied consequently. Finally, for pairs of diametral equal loads with the same load area, $A_n^m = B_n^m = 0$ holds for all odd n.

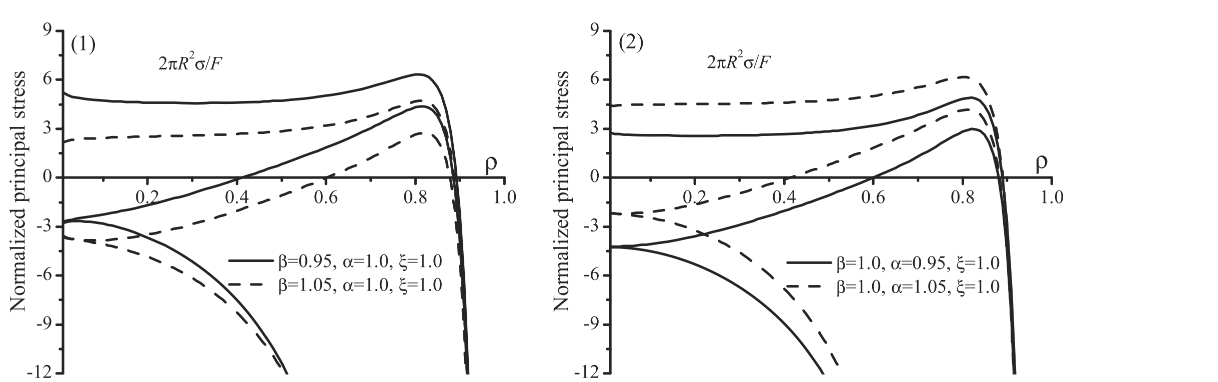

Fig. 9. Normalized principal stress along one loading axis for anisotropic materials: (1) $\beta = 0.95$ or 1.05, $\alpha = 1.0$, $\xi = 1.0$; (2) $\beta = 1.0$, $\alpha = 0.95$ or 1.05, $\xi = 1.0$. The load configuration and ϕ_i, ν are the same with $N_c = 4$ as in Fig. 8.

The solution of Hiramatsu and Oka (1966) can be regarded as a special case of the solution of Chau and Wei (1999). Our solution obtained in this work is an extension of the solution of Chau and Wei (1999). Note that Wijk (1978) speculated on the invalidity of applying the solution from Hiramatsu and Oka (1966) in the vicinity of the load areas. The applicability of such solutions is therefore discussed in the next section.

4. Some aspects about the application of the proposed solution

In this section, we discuss the applicability of the solution obtained in this work. However, the conclusions will also hold for the solutions of Hiramatsu and Oka (1966) and Chau and Wei (1999). The discussion includes two aspects. The first one is the convergence rate of the solution. For convenience the stress σ, which can denote any stress component of Eqs. (53)–(56), can be written for isotropic materials as

$$\sigma_n = \sum_{m=0}^{n} \sigma_{nm}, \quad \sigma = \sigma_0 + \sum_{n=2}^{\infty} \sigma_n, \tag{59}$$

where σ_n is the nth term in the series. The numerical evaluation is carried out by summing a finite number of terms. The number N_t is of concern as to the accuracy of the results. A fast convergence rate leads to less terms to achieve a certain accuracy. Fig. 10 shows values of nth term of the normalized stress $\sigma_{\theta\theta}$ at various positions ρ plotted versus the even number n at which the series has been truncated. This corresponds to an elastic sphere subjected to a pair of diametral loads with Hertz pressures where $v = 0.25$ and $\phi_1 = \phi_2 = 5°$. The terms for odd n are equal to zero because of load symmetry and not counted into N_t in this work. The maximum tensile stress appearing around $\rho = 0.81$ requires about $N_t = 20$ to achieve a relative error of less than 0.1%. However, more terms are needed with ρ approaching 1. In other words, the convergence rate at points near the surface becomes slow. For example, to achieve the same relative error of 0.1%, the numerical evaluations show that $N_t \approx 140$ at $\rho = 0.95$ while $N_t \approx 320$ at $\rho = 0.99$.

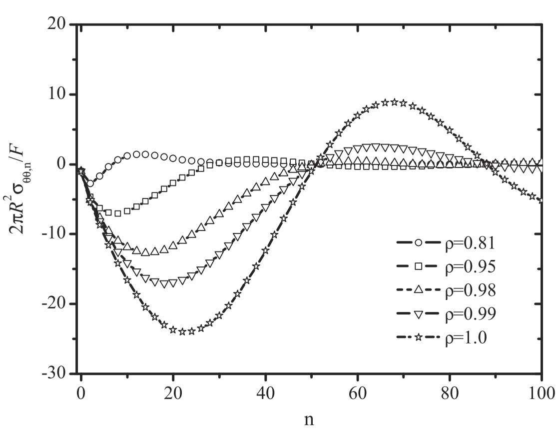

Fig. 10. Truncated normalized stress $\sigma_{\theta\theta,n}$ versus truncation number n plotted for various positions ρ along the loading axis as calculated from our solution for $N_c = 2$ and Hertz pressure. $v = 0.25$ and $\phi_1 = \phi_2 = 5°$.

The second aspect is the applicability of our solution on the sphere surface. Fig. 10 illustrates that the slowest convergence rate is found on the surface ($\rho = 1$). If good convergence, such as a relative error less than 1%, can be achieved only when N_t is very large, this might lead to numerical problems. Fig. 11 shows the stresses on the surface derived from three methods with parameter sets as used in the last section for Table 1. The stresses are plotted with respect to the normalized distance away from the center of the contact area. The Hüber–Hertz result is obtained by applying $z = 0$ in the solution of Hüber (1904). The normalized maximum tensile stress appearing around $\rho_1 = 1$ is 66 corresponding to 420 MPa. The maximum tensile stress with $N_t = 2000$ terms for our solution is 49.4. The relative change, compared to $N_t = 8000$, is less than 2%. This value is still much smaller than 66. In the FEM simulations, three mesh sizes, namely 0.125, 0.25 and 0.5 μm, on the surface are used, respectively. The derived maximum tensile stress becomes higher with smaller mesh size. Its position approaches to $\rho_1 = 1$ with decreasing mesh size. The maximum normalized tensile stress for the mesh size of 0.125 μm is only about 39.5. Except for the area around $\rho_1 = 1$, the stresses from FEM simulations and our solution are a little higher than the Hüber–Hertz result. Even so, both FEM results and our solution agree well with each other in most of the surface. This proves the applicability of our solution even on the surface. In comparing the curves in Fig. 11, it has to be kept in mind that the stresses from the Hüber–Hertz solution are derived in a cylindrical coordinate system referring to a deformed state of the sphere, while the stresses from our solution and the FEM simulation are given in a spherical coordinate system referring to an undeformed state of the sphere.

As for the maximum principal or tensile stresses on the surface, there are three different values derived from our solution, FEM simulations and the Hüber–Hertz solution, respectively. It is probable that the convergence rate near the point, $\rho_1 = 1$, in our solution is too slow. Only summing nearly infinite terms could then achieve a good accuracy. In this case, the maximum tensile stress evaluated with a finite number would be underestimated. Besides, the numerical integral in Eq. (47) for big n may be not accurate anymore. As a result, there will be a numerical problem to evaluate the maximum tensile stress around $\rho_1 = 1$. As for the FEM simulations, in view of the high stress gradient around $\rho_1 = 1$, it is not

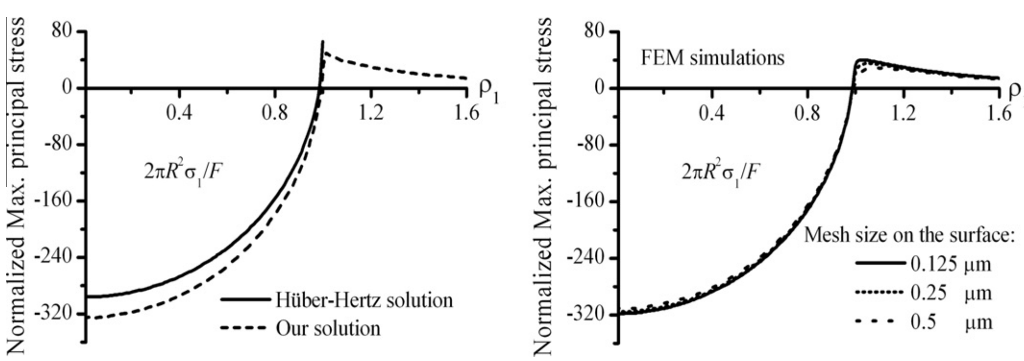

Fig. 11. Normalized maximum principal stress on the surface, $\rho_1 = R\sin\phi/R_a$ for the Hüber–Hertz solution and $\rho_1 = R\phi/R_a$ for FEM simulations and our solution and ϕ is shown in Fig. 4. Values of R, E, v, F are the same as those stated in the last section.

strange that the maximum tensile stresses depend on the mesh size to some extent. This does not mean that there is a stress singularity. The stresses from FEM simulations will be always underestimated with a finite mesh size in principle. Thus, for the calculation of stresses on the surface in the neighbourhood of $\rho_1 = 1$, the Hüber–Hertz solution is preferred. As for stress analysis, all stress components in a sphere can be numerically evaluated. The required information for our solution includes the load positions and ϕ_i or load areas. The spherical coordinate system can be selected almost arbitrarily. The only requirement on the coordinate system is that every load lies within $\phi_i < \theta_i < \pi - \phi_i$ (see Appendix C). The load areas can be obtained from experiments or Hertz theory. For the Hertz theory, it is assumed that the load area is independent of the other loads. By now, all stresses in a sphere can be estimated with our solution. For example, the stresses in spherical pebbles in crush tests ($N_c = 2$, see Fig. 1) can be analyzed by the following steps. First, the load positions have to be specified like (θ,φ) and $(\pi - \theta, \varphi + \pi)$ where θ and φ can be arbitrary angles. Secondly, the load areas measured from experiments are converted to ϕ_1 and ϕ_2. Finally, the stresses under consideration can be solved by our solution with θ, φ, ϕ_1 and ϕ_2. Note that the stresses along $\theta = 0$ and $\theta = \pi$ are not available in our solution because of the artificial singularity, e.g., $\sigma_{r\varphi}$ in Eq. (54) and $\sigma_{\theta\varphi}$ in Eq. (56). This may not be a problem as an appropriate coordinate system can be normally found. The Hüber–Hertz solution is preferred to calculate the stresses at points around $\rho_1 = 1$ for elastic contacts. For a sphere compressed by various loads, i.e., $N_c > 2$, stress analysis can be performed with a similar procedure as in the above example.

5. Some considerations on pebble failure

It is often regarded that a brittle particle will fail when the maximum tensile stress inside the particle reaches its critical strength, e.g., Jaeger (1967), Kschinka et al. (1986), and Chau et al. (2000). In view of this failure criterion, it is of significance that our results show that N_c may affect stresses inside spheres to some extent. On the other hand, failure of brittle spheres was found to be dominated by the maximum shear stress (Russell et al., 2009). Table 1 shows that maximum shear stresses appear close to the load area. As shown in Figs. 7 and 8, stresses close to the surface are not influenced by N_c. This means failure of brittle particles will only depend on the maximum contact force, e.g., Marketos and Bolton (2007). In this case, N_c has no impact on failure. Similar, if it is assumed that the maximum tensile stress on the sphere surface as shown in Fig. 11 dominates pebble failure, N_c will have no influence on failure, either. It is thus very important to apply a suitable failure criterion for a particular brittle particle under consideration. As for pebbles, we will publish related work in a later article.

There are few experiments to study the influence of N_c on the failure of spherical particles. For instance, Couroyer et al. (2000) reported the crush load distribution of alumina beads between a flat plate and an assembly of fixed steel beads. In this case, the maximum tensile stress in these beads can be calculated using our solution, as long as pressure distribution is adjusted to the contact conditions (e.g., elastic or plastic). Failure criteria can be developed or validated using such experimental results and our analytical solution.

6. Conclusions

In this paper, an analytical solution for the stresses in an elastic sphere subjected to arbitrary surface loads is derived. The stresses in the sphere have been obtained by summing a finite number of terms in the solution. Two kinds of pressure distribution, uniform and Hertz pressure, are applied in the load areas. The stresses derived with Hertz pressure agree well with the results from FEM simulations where a sphere is compressed by two parallel elastic plates. Other pressure distributions in real contact, may they be obtained by experiment, theory or simulation, can be applied to our analytical solution as well. The numerical evaluation of our solution clearly shows the influence of the coordination number N_c of load on stresses inside the sphere. N_c has to be taken into account when the stresses inside a sphere are of big concern.

Our solution can be applied at any points in a sphere in principle. However, a large number of terms needs to be added up to achieve a good accuracy at surface points around the boundary of the load area. The Hüber–Hertz solution is then preferred to calculate the stresses at these points.

Acknowledgments

This work is supported by the scholarship program CSC-HGF (China Scholarship Council (CSC) and Helmholtz Association of German Research Centres (HGF)) and the programme FUSION of Karlsruhe Institute of Technology (KIT). This work has been carried out at Institute of Applied Materials (IAM, former IMF II) of KIT.

Appendix A. Displacement potential functions

The procedure to derive the displacement potential functions Z and Φ as done by Chau and Wei (1999) is described below.

Hu (1954) proposed that the displacement potential under consideration can be resolved into two parts

$$u_r = u_r^I + u_r^{II} = 0 + w, \tag{A.1}$$

$$u_\theta = u_\theta^I + u_\theta^{II} = -\frac{1}{r\sin\theta}\frac{\partial\Psi}{\partial\varphi} - \frac{1}{r}\frac{\partial G}{\partial\theta}, \tag{A.2}$$

$$u_\varphi = u_\varphi^I + u_\varphi^{II} = \frac{1}{r}\frac{\partial\Psi}{\partial\theta} - \frac{1}{r\sin\theta}\frac{\partial G}{\partial\varphi}, \tag{A.3}$$

where Ψ and G are two displacement functions. Substitution of the above equations into Eqs. (4) and (6) subsequently yields

$$\frac{2(a+b)}{r^3}\nabla_1^2 G - \frac{d}{r^2}\nabla_1^2\frac{\partial G}{\partial r} + \frac{2g}{r^2}w + \frac{c}{r^2}\frac{\partial}{\partial r}\left(r^2\frac{\partial w}{\partial r}\right) + \frac{h}{r^2}\nabla_1^2 w = 0, \tag{A.4}$$

$$\frac{1}{r}\frac{\partial B}{\partial\theta} + \frac{1}{r\sin\theta}\frac{\partial A}{\partial\varphi} = 0, \quad \frac{1}{r}\frac{\partial A}{\partial\theta} - \frac{1}{r\sin\theta}\frac{\partial B}{\partial\varphi} = 0, \tag{A.5}$$

where

$$\begin{aligned} A &= -\frac{a}{r^2}\nabla_1^2 G + \frac{2b}{r^2}G - h\frac{\partial^2 G}{\partial r^2} + \frac{2(a+b)}{r}w + d\frac{\partial w}{\partial r}, \\ B &= (h-b)\left(\frac{1}{r^2}\nabla_1^2\Psi + \frac{2\Psi}{r^2}\right) + h\left(\frac{\partial^2\Psi}{\partial r^2} - \frac{2\Psi}{r^2}\right), \end{aligned} \tag{A.6}$$

$$\begin{aligned} &a = A_{12} + 2A_{66}, \quad b = A_{44} - A_{66}, \quad c = A_{33} \\ &d = A_{13} + A_{44}, \quad h = A_{44}, \quad g = d + h - 2(a+b). \end{aligned} \tag{A.7}$$

It has been proved that both A and B can be set to zero:

$$A = 0, \quad B = 0. \tag{A.8}$$

The following change of variables is introduced

$$r = Re^\eta, \quad \Psi = RZe^\eta, \quad G = RFe^\eta, \quad w = -r\frac{\partial H}{\partial r} = -\frac{\partial H}{\partial\eta}, \tag{A.9}$$

where Z, F and H are displacement functions with respect to the dimensionless radial variable η.

Substitution of the above variables into Eqs. (A.4), (A.6) and (A.8) yields Eq. (18)

$$A_{44}\left(\frac{\partial^2 Z}{\partial\eta^2}+\frac{\partial Z}{\partial\eta}\right)+A_{66}\nabla_1^2 Z-2(A_{44}-A_{66})Z=0$$

and

$$\left[h\left(\frac{\partial^2}{\partial\eta^2}+\frac{\partial}{\partial\eta}\right)+a\nabla_1^2-2b\right]F+\left[d\frac{\partial^2}{\partial\eta^2}+2(a+b)\frac{\partial}{\partial\eta}\right]H=0, \tag{A.10}$$

$$\left[(h-g)\nabla_1^2-d\nabla_1^2\frac{\partial}{\partial\eta}\right]F-\left[c\left(\frac{\partial^3}{\partial\eta^3}+\frac{\partial^2}{\partial\eta^2}\right)+h\nabla_1^2\frac{\partial}{\partial\eta}+2g\frac{\partial}{\partial\eta}\right]H=0. \tag{A.11}$$

Another displacement function ϕ is introduced to uncouple F and H in Eqs. (A.10) and (A.11):

$$F=\left[d\frac{\partial^2}{\partial\eta^2}+2(a+b)\frac{\partial}{\partial\eta}\right]\phi, \tag{A.12}$$

$$H=-\left[h\left(\frac{\partial^2}{\partial\eta^2}+\frac{\partial}{\partial\eta}\right)+a\nabla_1^2-2b\right]\phi. \tag{A.13}$$

It can be seen that such ϕ does satisfy Eq. (A.10). Substitution of Eqs. (A.12) and (A.13) into Eq. (A.11) leads to Eq. (19), i.e.,

$$\left[\begin{array}{c}\left(\frac{\partial^2}{\partial\eta^2}+\frac{\partial}{\partial\eta}\right)^2+2D\left(\frac{\partial^2}{\partial\eta^2}+\frac{\partial}{\partial\eta}\right)+M\nabla_1^2\left(\frac{\partial^2}{\partial\eta^2}+\frac{\partial}{\partial\eta}\right)\\ -4L+2(N-L)\nabla_1^2+N\nabla_1^2\nabla_1^2\end{array}\right]\Phi=0,$$

where

$$D=\frac{hg-bc}{ch},\quad L=\frac{bg}{ch},\quad M=\frac{ac+h^2-d^2}{ch},\quad N=\frac{a}{c} \tag{A.14}$$

and Φ is defined as

$$\Phi=-\frac{\partial\phi}{\partial\eta}. \tag{A.15}$$

Subsequently, the displacement functions can be expressed by Z and Φ, i.e., Eq. (20).

Appendix B. Fourier associated Legendre series

For the asymmetric and piecewise boundary condition at the complete surface of the sphere the pressure function $p(\theta,\varphi)$ $(0\leqslant\theta\leqslant\pi,\ 0\leqslant\varphi\leqslant 2\pi)$, can be expanded with the orthogonal functions

$$\Big\{P_n^m(\cos\theta)\cos m\varphi\ (n\geqslant 0, n\geqslant m\geqslant 0),\quad P_k^l(\cos\theta)\sin l\varphi\ (k>0, k\geqslant l>0)\Big\}, \tag{B.1}$$

where P_n^m and P_k^l are the associated Legendre functions, and n, m, k, l are integers. The orthogonality relations for any two functions in the above system are

$$\int_0^\pi\int_0^{2\pi}P_n^m(\cos\theta)\cos m\varphi P_k^l(\cos\theta)\sin l\varphi\sin\theta\, d\varphi\, d\theta=0, \tag{B.2}$$

$$\int_0^\pi\int_0^{2\pi}\left(P_n^m(\cos\theta)\cos m\varphi\right)^2\sin\theta\, d\varphi\, d\theta=\frac{2\pi\delta_m(n+m)!}{(2n+1)(n-m)!}, \tag{B.3}$$

$$\int_0^\pi\int_0^{2\pi}\left(P_k^l(\cos\theta)\sin l\varphi\right)^2\sin\theta\, d\varphi\, d\theta=\frac{2\pi(k+l)!}{(2k+1)(k-l)!}, \tag{B.4}$$

where $\sin\theta$ is a weight function and

$$\delta_m=\begin{cases}2 & m=0,\\ 1 & m\neq 0.\end{cases} \tag{B.5}$$

So the function p can be expanded as

$$p(\theta,\varphi)=\sum_{n=0}^{\infty}\sum_{m=0}^{m=n}\left(A_n^m\cos m\varphi+B_n^m\sin m\varphi\right)P_n^m(\cos\theta), \tag{B.6}$$

where

$$\begin{aligned}A_n^m&=\frac{(2n+1)(n-m)!}{2\pi\delta_m(n+m)!}\int_0^\pi\int_0^{2\pi}p(\theta,\varphi)P_n^m(\cos\theta)\cos m\varphi\sin\theta\, d\varphi\, d\theta,\\ B_n^m&=\frac{(2n+1)(n-m)!}{2\pi(n+m)!}\int_0^\pi\int_0^{2\pi}p(\theta,\varphi)P_n^m(\cos\theta)\sin m\varphi\sin\theta\, d\varphi\, d\theta.\end{aligned} \tag{B.7}$$

Appendix C. The domain of integration

The load circle S_i, is represented by an ellipse in the left sketch of Fig. C.1. O_i is the center of the load circle corresponding to (Rcos $\phi_i,\theta_i,\varphi_i$) in the spherical coordinate system, where R is the sphere radius. The spherical load circle subtends an angle of $2\phi_i$. O is the center of the sphere and P is a point in the z-axis. O_i' is the projection of O_i in the x–y plane. The line across the points O_i and P lies in the plane containing the load circle. The plane across the points O, P and O_i is perpendicular to the load circle. The points Q_1 and Q_2 corresponding to the same θ locate at the edge of S_i. The line across the points Q_1 and Q_2 is parallel to the x–y plane. Q_1' and Q_2' in the right sketch are the projections of Q_1 and Q_2 in the x–y plane. It is aimed to find the function $\varphi_0(\theta)$.

Care should be taken that the spherical coordinate system must be appropriately chosen so that every load lies in $\phi_i<\theta_i<\pi-\phi_i$. Otherwise, if the z-axis goes through the inner of load circle, the following construction will not work. Nevertheless, an appropriate coordinate system can be normally found in case of a limited coordination number and a small load area. The coordination number is limited for spheres with a similar size. For example, the maximum coordination number in a three dimensional space is 12 for mono-sized spheres. Besides, for ceramic spherical pebbles compressed by plates, the ϕ_i which is related to the ith load area is relatively small before failure occurs. Therefore, it will not be a big issue to identify an appropriate coordinate system. The geometrical relations read as

$$\begin{aligned}&b=R\sin\phi_i,\quad h=R\cos\phi_i,\quad c=h|\tan\theta_i|,\ f=h|\sec\theta_i|,\\ &d=\sqrt{R^2+f^2-2Rf|\cos\theta|},\quad p=\frac{b+c+d}{2},\\ &e=\frac{2\sqrt{p(p-c)(p-b)(p-d)}}{c},\\ &m=R\sin\theta,\quad \varphi_0(\theta)=\arcsin\frac{e}{m}.\end{aligned} \tag{C.1}$$

There is a special case for the load area with $\theta_i=\pi/2$. In this case,

$$\varphi_0(\theta)=\arcsin\frac{\sqrt{b^2-(R\cos\theta)^2}}{m}=\frac{\sqrt{\sin^2\phi_i-\cos^2\theta}}{\sin\theta}. \tag{C.2}$$

As a result, the integral domain is $[\theta_i-\theta_0,\theta_i+\theta_0]$ and $[\varphi_i-\varphi_0(\theta),\varphi_i-\varphi_0(\theta)]$.

Appendix D. Hertz pressure distribution

The Hertz pressure in Eq. (11) is expressed as a function of ϕ while the coefficients, A_n^m and B_n^m in Eq. (47) are derived with the pressure in terms of (θ,φ). Therefore, it is essential to obtain the

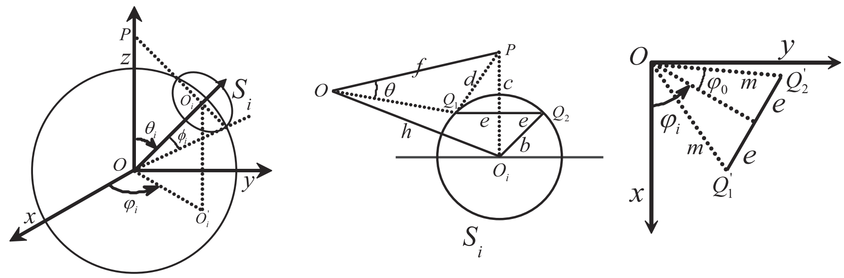

Fig. C.1. The domain of the load area.

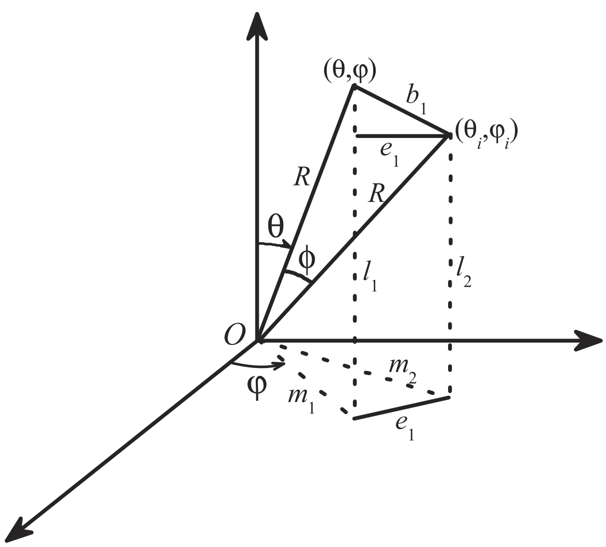

Fig. D.1. The acute angle between the lines (r,θ,φ) and (r,θ_i,φ_i).

angle between (r,θ_i,φ_i) and (r,θ,φ). Note that for any point (R,θ,φ) in the load area, $|\varphi-\varphi_i|$ is much smaller than $\pi/2$ because the load normally is very small. Accordingly, $0<\phi\ll\pi/2$ (see Fig. D.1).

$$m_1=R\sin\theta,\quad l_1=R|\cos\theta|,\quad m_2=R\sin\theta_i,\quad l_2=R|\cos\theta_i|, \tag{D.1}$$

$$\begin{aligned} e_1&=\sqrt{m_1^2+m_2^2-2m_1m_2\cos(|\varphi-\varphi_i|)}\\ &=R\sqrt{\sin^2\theta+\sin^2\theta_i-2\sin\theta\sin\theta_i\cos(|\varphi-\varphi_i|)}, \end{aligned} \tag{D.2}$$

$$\begin{aligned} b_1&=\sqrt{(l_1-l_2)^2+e_1^2}\\ &=R\sqrt{2}\sqrt{1-|\cos\theta\cos\theta_i|-\sin\theta\sin\theta_i\cos(|\varphi-\varphi_i|)}. \end{aligned} \tag{D.3}$$

The angle between the line (r,θ,φ) and the line (r,θ_i,φ_i) is

$$\phi(\theta,\varphi,\theta_i,\varphi_i)=2\arcsin\left(\frac{b_1}{2R}\right). \tag{D.4}$$

Appendix E. The relations between coefficients in the general solution and the boundary condition

The shear stress is 0 at any point on sphere surface. It is thus independent of θ and φ. For $\sigma_{r\varphi}|_{r=R}=\sigma_{r\varphi}|_{\rho=1}=0$, the independence of θ yields

$$D_{h1}^m(\lambda_{h1}-1)\cos m\varphi+D_{h2}^m(\lambda_{h2}-1)\sin m\varphi=0, \tag{E.1}$$

$$-(C_{l1}^mT_{l1}+C_{l2}^mT_{l2})\sin m\varphi+(C_{l3}^mT_{l1}+C_{l4}^mT_{l2})\cos m\varphi=0, \tag{E.2}$$

$$-\Pi(R_{n1}^m,I_{n1}^m)\sin m\varphi+\Pi(R_{n2}^m,I_{n2}^m)\cos m\varphi=0 \tag{E.3}$$

and for $\sigma_{r\theta}|_{r=R}=\sigma_{r\theta}|_{\rho=1}=0$, the independence of θ yields

$$-D_{h1}^m(\lambda_{h1}-1)\sin m\varphi+D_{h2}^m(\lambda_{h2}-1)\cos m\varphi=0, \tag{E.4}$$

$$(C_{l1}^mT_{l1}+C_{l2}^mT_{l2})\cos m\varphi+(C_{l3}^mT_{l1}+C_{l4}^mT_{l2})\sin m\varphi=0, \tag{E.5}$$

$$\Pi(R_{n1}^m,I_{n1}^m)\cos m\varphi+\Pi(R_{n2}^m,I_{n2}^m)\sin m\varphi=0, \tag{E.6}$$

where $T_{li}=(1-\mu_{li})\Gamma_{li}+\Lambda_{li}$ $(i=1,2)$. For Eqs. (E.1) and (E.4), the independence of φ yields

$$D_{h1}^m(\lambda_{h1}-1)=0,\quad D_{h2}^m(\lambda_{h2}-1)=0, \tag{E.7}$$

however, λ_h depends on h. As a result

$$D_{h1}^m=0,\quad D_{h2}^m=0. \tag{E.8}$$

For Eqs. (E.2) and (E.5), the independence of φ yields

$$\begin{cases} C_{l1}^mT_{l1}+C_{l2}^mT_{l2}=0,\\ C_{l3}^mT_{l1}+C_{l4}^mT_{l2}=0, \end{cases} \tag{E.9}$$

which implies

$$C_{l1}^m=-\frac{T_{l2}}{T_{l1}}C_{l2}^m=L_{l12}C_{l2}^m,\quad C_{l3}^m=-\frac{T_{l2}}{T_{l1}}C_{l2}^m=L_{l12}C_{l4}^m. \tag{E.10}$$

For Eqs. (E.3) and (E.6), the independence of φ yields

$$\Pi(R_{n1}^m,I_{n1}^m)=0,\quad \Pi(R_{n2}^m,I_{n2}^m)=0, \tag{E.11}$$

which implies

$$I_{n1}^m=\frac{\Pi(1,0)}{\Pi(0,-1)}=K_{n12}R_{n1}^m,\quad I_{n2}^m=\frac{\Pi(1,0)}{\Pi(0,-1)}=K_{n12}R_{n2}^m. \tag{E.12}$$

σ_{rr} can be obtained by replacing A_{12}, $(2A_{66})$ and A_{13} in Eq. (40) by A_{13}, 0 and A_{33}. For $\rho=1$, σ_{rr} read as

$$\begin{aligned} \sigma_{rr}=&-\frac{1}{R}\sum_l\sum_{m=0}^{l}\begin{bmatrix}(C_{l1}^mJ_{l1}+C_{l2}^mJ_{l2})\cos m\varphi\\ +(C_{l3}^mJ_{l1}+C_{l4}^mJ_{l2})\sin m\varphi\end{bmatrix}P_l^m(\cos\theta)\\ &+\frac{1}{R}\sum_n\sum_{m=0}^{n}[\Omega_1(R_{n1}^m,I_{n1}^m)\cos m\varphi\\ &+\Omega_1(R_{n2}^m,I_{n2}^m)\sin m\varphi]P_n^m(\cos\theta), \end{aligned} \tag{E.13}$$

where Eq. (E.8) has been used. Applying the boundary condition, $\sigma_{rr}|_{r=R}=\sigma_{rr}|_{\rho=1}=p(\theta,\varphi)$, yields

$$\begin{cases} C_{l1}^mJ_{l1}+C_{l2}^mJ_{l2}=-A_l^mR,\\ C_{l3}^mJ_{l1}+C_{l4}^mJ_{l2}=-B_l^mR \end{cases} \tag{E.14}$$

and

$$\begin{cases} \Omega_1(R_{n1}^m,I_{n1}^m)=A_n^mR,\\ \Omega_1(R_{n2}^m,I_{n2}^m)=B_n^mR. \end{cases} \tag{E.15}$$

The coefficients, C_{li}^{m} $(i = 1, 2, 3, 4)$, can be derived from the set of equations of (E.9) and (E.14). The coefficients, (R_{nk}^{m}, I_{n2}^{m}) $(k = 1, 2)$, can be derived from the set of equations of (E.11) and (E.15).

References

Boccaccini, L., Salavy, J.-F., Bede, O., Neuberger, H., Ricapito, I., Sardain, P., Sedano, L., Splichal, K., 2009. The EU TBM systems: design and development programme. Fusion Engineering and Design 84 (2–6), 333–337.

Chau, K.T., 1995. Bifurcations at a spherical cavity in a compressible solid with spherical isotropy. International Journal of Numerical and Analytical Methods in Geomechanics 19 (6), 381–398.

Chau, K.T., 1998. Toroidal vibrations of anisotropic spheres with spherical isotropy. Journal of Applied Mechanics 65, 59–65.

Chau, K.T., Wei, X.X., 1999. Spherically isotropic, elastic spheres subject to diametral point load strength test. International Journal of Solids and Structures 36 (29), 4473–4496.

Chau, K.T., Wei, X.X., Wong, R.H.C., Yu, T.X., 2000. Fragmentation of brittle spheres under static and dynamic compressions: experiments and analyses. Mechanics of Materials 32 (9), 543–554.

Chen, W.T., 1966. On some problems in spherically isotropic elastic materials. Journal of Applied Mechanics 33, 539–546.

Couroyer, C., Ning, Z., Ghadiri, M., 2000. Distinct element analysis of bulk crushing: effect of particle properties and loading rate. Powder Technology 109 (1–3), 241–254.

Dean, W., Sneddon, I., Parsons, H., 1952. Selected Government Research Reports: Strength and Testing of Materials: Part II: Testing Methods and Test Results.

Ding, H.-J., Ren, Y.-J., 1991. Equilibrium problems of spherically isotropic bodies. Applied Mathematics and Mechanics 12, 155–162.

Gan, Y., Kamlah, M., 2010. Discrete element modelling of pebble beds: with application to uniaxial compression tests of ceramic breeder pebble beds. Journal of the Mechanics and Physics of Solids 58 (2), 129–144.

Giancarli, L., Ferrari, M., Fütterer, M., Malang, S., 2000. Candidate blanket concepts for a European fusion power plant study. Fusion Engineering and Design 49–50, 445–456.

Guerrero, I., Turteltaub, M.J., 1972. The elastic sphere under arbitrary concentrated surface loads. Journal of Elasticity 2, 21–33.

Gundepudi, M.K., Sankar, B.V., Mecholsky, J.J., Clupper, D.C., 1997. Stress analysis of brittle spheres under multiaxial loading. Powder Technology 94 (2), 153–161.

Hertz, H., 1881. Über die Berührung fester elastischer Körper. Journal für die reine und Angewandte Mathematik 92, 156–171.

Hiramatsu, Y., Oka, Y., 1966. Determination of the tensile strength of rock by a compression test of an irregular test piece. International Journal of Rock Mechanics and Mining Sciences 3 (2), 89–90.

Hu, H.-C., 1954. On the general theory of elasticity for a spherically isotropic medium. Acta Scientia Sinica 3, 247–260.

Hüber, M.T., 1904. Zur Theorie der Berührung fester elastischer Körper. Annalen der Physik 319, 153–163.

Jaeger, J.C., 1967. Failure of rocks under tensile conditions. International Journal of Rock Mechanics and Mining Science 4 (2), 219–227.

Johnson, K.L., 1987. Contact Mechanics. Cambridge University Press.

Knitter, R., 2003. Quality control of lithium orthosilicate pebbles and long-term annealing behaviour of ceramic breeder materials. Report on tw2-ttbb-002b-d2, fzk fusion nr. 220.

Knitter, R., Alm, B., Roth, G., 2007. Crystallisation and microstructure of lithium orthosilicate pebbles. Journal of Nuclear Materials 367-370 (Part 2), 1387–1392.

Kschinka, B.A., Perrella, S., Nguyen, H.C.B.R., 1986. Strengths of glass spheres in compression. Journal of the American Ceramic Society 69 (6), 467–472.

Löbbecke, B., Knitter, R., 2009. Procurement and quality control of Li_4SiO_4 pebbles for testing of breeder unit mock-ups-OSi 08. Forschungszentrum Karlsruhe 338.

Marketos, G., Bolton, M.D., 2007. Quantifying the extent of crushing in granular materials: a probability-based predictive method. Journal of the Mechanics and Physics of Solids 55 (10), 2142–2156.

Poitevin, Y., Boccaccini, L., Cardella, A., Giancarli, L., Meyder, R., Diegele, E., Laesser, R., Benamati, G., 2005. The European breeding blankets development and the test strategy in ITER. Fusion Engineering and Design 75–79, 741–749.

Russell, A.R., Muir Wood, D., 2009. Point load tests and strength measurements for brittle spheres. International Journal of Rock Mechanics and Mining Sciences 46 (2), 272–280.

Russell, A.R., Muir Wood, D., Kikumoto, M., 2009. Crushing of particles in idealised granular assemblies. Journal of the Mechanics and Physics of Solids 57 (8), 1293–1313.

Tsuchiya, K., Kawamura, H., Takayama, T., Kato, S., 2005. Control of particle size and density of Li_2TiO_3 pebbles fabricated by indirect wet processes. Journal of Nuclear Materials 345 (2–3), 239–244.

van der Laan, J., Muis, R., 1999. Properties of lithium metatitanate pebbles produced by a wet process. Journal of Nuclear Materials, 401–404.

Vollath, D., Wedemeyer, H., Zimmermann, H., Werle, H., 1990. Doped lithium orthosilicate: preparation and properties. Journal of Nuclear Materials 174 (1), 86–91.

Wijk, G., 1978. Some new theoretical aspects of indirect measurements of the tensile strength of rocks. International Journal of Rock Mechanics and Mining Sciences and Geomechanics Abstract 15 (4), 149–160.

Zhao, S., Gan, Y., Kamlah, M., Kennerknecht, T., Rolli, R., submitted for publication. Li_4SiO_4 pebbles in crush tests and evaluation of the contact strength in pebble–pebble contact. Engineering Fracture Mechanics.